A felsic meta-igneous source for Li-F-rich peraluminous granites: insights from the Variscan Velay dome (French Massif Central) and implications for rare-metal magmatism

Christophe Ballouard, Simon Couzinié, Pierre Bouilhol, Matthieu Harlaux, Julien Mercadier, Jean-Marc Montel

Contributions to Mineralogy and Petrology

A felsic meta-igneous source for Li-F-rich peraluminous granites: insights from the Variscan Velay dome (French Massif Central) and implications for rare-metal magmatism

--Manuscript Draft--

Manuscript Number:	CTMP-D-23-00068R2
Full Title:	A felsic meta-igneous source for Li-F-rich peraluminous granites: insights from the Variscan Velay dome (French Massif Central) and implications for rare-metal magmatism
Article Type:	Original Paper
Keywords:	Rare-metal granites; Crustal melting; Mineral/mineral element partitioning; Trace element geochemistry; Lithium-fluorine; Variscan orogeny
Corresponding Author:	Christophe Ballouard, Ph.D GeoRessources VANDOEUVRE-LES-NANCY, FRANCE
Corresponding Author Secondary Information:	
Corresponding Author's Institution:	GeoRessources
Corresponding Author's Secondary Institution:	
First Author:	Christophe Ballouard, Ph.D
First Author Secondary Information:	
Order of Authors:	Christophe Ballouard, Ph.D
	Simon Couzinié, PhD
	Pierre Bouilhol, PhD
	Matthieu Harlaux, PhD
	Julien Mercadier, PhD
	Jean-Marc Montel, PhD
Order of Authors Secondary Information:	
Funding Information:	LabEx Ressources 21 (ANR-10-LABX-21-RESSOURCES21) — Dr Christophe Ballouard
	Conseil régional du Grand Est (programme 'Jeunes chercheurs' 2020) — Dr Christophe Ballouard
	CNRS/INSU (TelluS-2022) — Dr Pierre Bouilhol
Abstract:	The Velay anatectic dome in the Variscan French Massif Central exposes a low pressure-high temperature metamorphic sequence, which represents an ideal natural laboratory for documenting the behavior of rare-metals and fluxing elements during crustal melting. We investigated the silicate and bulk-rock geochemistry of sub- to supra-solidus metapelites and orthogneisses, as well as related granites, and performed forward thermodynamically constrained geochemical modelling to quantify the respective effects of melting pressure, temperature, H2O activity, and protolith composition on the Li and F contents of granitic melts. We find that biotite compositions are good proxies of melt compositional evolutions during prograde melting. The crystallization of peritectic cordierite at low-pressure (< 5 kbar) and "water-fluxed" melting both inhibit the Li enrichment of anatectic melts. Metapelite-derived melts consistently show modest Li–F contents, and a decoupling is observed as melts with the highest Li concentrations (~200-400 ppm) are produced below 750°C, whereas F-richest melts (~0.2-0.4 wt%) are produced above 750°C near the biotite-out isograd. Peraluminous orthogneiss anatexis can generate a melt that is concomitantly enriched

	in both F (~0.3-1 wt%) and Li (~600-1350 ppm) at relatively low temperature (< 750°C), which can evolve towards rare-metal granite compositions (~10,000 ppm Li; ~2 wt% F) after 80–90 wt% of fractional crystallization. Melting of felsic meta-igneous rocks followed by magmatic differentiation is thus a viable mechanism to form Li-F-rich rare-metal granites and pegmatites, providing a direct link between protracted crust recycling and rare-metal magmatism in late-orogenic settings.
Response to Reviewers:	Dear Prof. Müntener – Executive editor, Our answers to your comments are provided in a specific file attached to our submission (Rebuttal letter-R2) and we also provide a specific version of the revised manuscript with changes highlighted in red and yellow (Manuscript with marked changes). Best regards, Christophe Ballouard, Simon Couzinié, Pierre Bouilhol, Matthieu Harlaux, Julien Mercadier, Jean-Marc Montel

Title: A felsic meta-igneous source for Li-F-rich peraluminous granites: insights from the Variscan Velay dome (French Massif Central) and implications for rare-metal magmatism

Authors: Christophe Ballouard[1*], Simon Couzinié[2], Pierre Bouilhol[2], Matthieu Harlaux[3], Julien Mercadier[1], Jean-Marc Montel[2]

[1] Université de Lorraine, CNRS, GeoRessources, 54000 Nancy, France

[2] Université de Lorraine, CNRS, CRPG, 54000 Nancy, France

[3] BRGM – French Geological Survey, 45060 Orléans, France

*Corresponding author: christophe.ballouard@univ-lorraine.fr; christopheballouard@outlook.com

Abstract

The Velay anatectic dome in the Variscan French Massif Central exposes a low pressure-high temperature metamorphic sequence, which represents an ideal natural laboratory for documenting the behavior of rare-metals and fluxing elements during crustal melting. We investigated the silicate and bulk-rock geochemistry of sub- to supra-solidus metapelites and orthogneisses, as well as related granites, and performed forward thermodynamically constrained geochemical modelling to quantify the respective effects of melting pressure, temperature, H_2O activity, and protolith composition on the Li and F contents of granitic melts. We find that biotite compositions are good proxies of melt compositional evolutions during prograde melting. The crystallization of peritectic cordierite at low-pressure (< 5 kbar) and "water-fluxed" melting both inhibit the Li enrichment of anatectic melts. Metapelite-derived melts consistently show modest Li–F contents, and a decoupling is observed as melts with the highest Li concentrations (~200-400 ppm) are produced below 750°C, whereas F-richest melts (~0.2-0.4 wt%) are produced above 750°C near the biotite-out isograd. Peraluminous

orthogneiss anatexis can generate a melt that is concomitantly enriched in both F (~0.3-1 wt%) and Li (~600-1350 ppm) at relatively low temperature (< 750°C), which can evolve towards rare-metal granite compositions (~10,000 ppm Li; ~2 wt% F) after 80–90 wt% of fractional crystallization. Melting of felsic meta-igneous rocks followed by magmatic differentiation is thus a viable mechanism to form Li-F-rich rare-metal granites and pegmatites, providing a direct link between protracted crust recycling and rare-metal magmatism in late-orogenic settings.

Key words

Rare-metal granites; Crustal melting; Mineral/mineral element partitioning; Trace element geochemistry; Lithium-fluorine; Variscan orogeny

Introduction

Major hard-rock deposits of Li and other rare-metals (Sn, Ta, Nb, Cs and Be) strategic for the high-technology industry and the energy transition are associated with low-volume (typically < 1 km^3) highly peraluminous leucogranite and pegmatite intrusions, which formed in relation with crustal magmatism in late-orogenic setting since the Mesoarchean (Linnen et al. 2012; Gourcerol et al. 2019). Peraluminous high phosphorous rare-metal granites and LCT (Li-Cs-Ta-rich) pegmatites (RMGP) typically host a disseminated mineralization of Li (e.g., lepidolite-zinnwaldite, spodumene, petalite, Li-phosphates), Nb-Ta (columbite- or pyrochlore-group minerals), Sn (cassiterite), Be (beryl), and F (topaz). They may exhibit incompatible and fluxing (F-Li) element concentrations up to three orders of magnitude higher than other types of peraluminous granites (Černý and Ercit 2005; Linnen and Cuney 2005; Romer and Pichavant 2021).

Magmatic-hydrothermal processes including fluid-melt immiscibility and alkali metasomatism may lead to significant enrichments and redistributions of rare-metals at the end

of the crystallization of granitic and pegmatitic intrusions (Harlaux et al. 2017; Kaeter et al. 2018; Ballouard et al. 2020; Pfister et al. 2023). However, the occurrence of hypabyssal to volcanic analogues of RMGPs (Pichavant et al. 1987, 1988; Raimbault and Burnol 1998) as well as experimental studies (Linnen and Cuney 2005; Pichavant 2022) indicate that their rare-metal enrichment is dominantly a primary magmatic feature. The geological processes leading to the formation of such rare-metal and flux-rich granitic melts remain controversial. The RMGPs are generally interpreted as residual silicate melts produced by extreme fractionation (≥ ~99 wt%) of less evolved peraluminous felsic magmas ("residual model": Černý et al. 2005; Hulsbosch et al. 2014; London 2018; Roda-Robles et al. 2018). The latter model is hampered by the common lack of spatial and/or temporal relations between RMGPs and their parental granitic sources, and alternative models involve low-degree of crustal partial melting and/or suitable pre-enriched protoliths ("anatectic model": Stewart 1978; Müller et al. 2017; Knoll et al. 2018, 2023; Konzett et al. 2018; Gourcerol et al. 2019).

Those two models are not mutually exclusive and the formation of RMGPs could result from the local superimposition of geologic processes occurring at different spatial-temporal scales and in distinct tectonic settings (Romer and Pichavant 2021). Of peculiar importance is the weathering-related enrichment of rare-metals such as Sn, W or Li in siliciclastic sedimentary protoliths (i.e., sedimentary recycling) before tectonic stacking and partial melting in collisional orogens (Romer and Kroner 2015, 2016). Additionally, polycyclic crustal evolution involving re-melting of granites combined with magmatic differentiation could ultimately lead to the generation of fertile meta-igneous protoliths for RMGPs (Černý 1989), as proposed for U-rich leucogranites (Turpin et al. 1990; Ballouard et al. 2018).

Micas represent major hosts for rare-metals and halogen elements in aluminous metamorphic rocks and mica-breakdown melting reactions are thus key to control rare-metal and fluxing element partitioning in granitic melts (Bea et al. 1994; Icenhower and London 1995;

Michaud et al. 2021). Lithium, Cs, Ta, and F are preferentially incorporated in biotite relative to muscovite, whereas the opposite is true for Be, Sn, and W (Kunz et al. 2022). As the dehydration-melting reaction of biotite occurs at higher temperature than that of muscovite (Vielzeuf and Holloway 1988; Patiño-Douce 1999; Weinberg and Hasalová 2015), the rare-metal budget of anatectic melts is controlled by: (i) the pressure-temperature conditions of partial melting and H_2O activity; (ii) the bulk metal concentration of the protolith; and (iii) its mineralogical composition, notably the amount of micas and the relative proportions of muscovite vs. biotite, impacting melting degree and residue-melt element partitioning at given P-T conditions. The dynamic of melt extraction from migmatitic sources can also affect the rare-metal concentrations of anatectic magmas. For example, low-temperature melts can be either enriched or depleted in certain elements, and the preservation of their rare-metal signatures will depend on their capacity to be extracted before dilution by higher temperature melts having different compositions (Wolf et al. 2018; Romer and Pichavant 2021).

Several studies argued that biotite-breakdown at T > 800°C is decisive for the generation of rare-metal-rich granitic melts (Simons et al. 2016; Wolf et al. 2018; Michaud et al. 2021; Kunz et al. 2022). However, the partitioning of rare-metals and halogens during crustal melting remains poorly understood, as some elements might be liberated in the melt at low or high temperature, as for example documented for W and Sn, respectively (Zhao et al. 2022). Besides, the influence of peritectic garnet and cordierite produced upon biotite breakdown on controlling the melt rare-metal endowment has yet to be fully investigated. Indeed, discrepancies exist between experimental and natural partitioning data for cordierite, Li being suggested either as compatible (Bea et al. 1994) or incompatible (Evensen and London 2003) in this mineral.

Furthermore, the dehydration of the lower crust induced by granulite-facies metamorphism could liberate metamorphic fluids enriched in F and mica-hosted metals, thus enhancing fluxed melting of the overlying crust and the formation of RMGP melts (Cuney and Barbey 2014).

However, there is scarce evidence for the circulation of such enriched fluids in the deep Variscan crust, and the impact of flux-melting on the rare-metal enrichment of silicate melts remains ill-defined.

To constrain the rare-metal and fluxing element partitioning during crustal anatexis, we undertook a silicate and bulk-rock geochemical study of the rocks composing the Velay anatectic dome (Variscan French Massif Central). This well-studied area exposes a low pressure-high temperature (LP-HT) prograde metamorphic sequence ranging from greenschists to migmatites and granites, and represents an ideal natural laboratory to document the behavior of rare-metals and fluxing elements upon crustal partial melting. We primarily focused on the partitioning of Li and F, two fluxing elements with different geochemical properties that would allow an appraisal of the behavior of other elements with economic interest (e.g., Nb, Ta, Sn, W, Be, Cs). By coupling our results with thermodynamically-constrained geochemical modeling, we quantify the respective effects of melting pressure, temperature, H_2O activity, and protolith composition on the Li and F contents of granitic melts. We conclude that peraluminous orthogneiss melting at relatively low temperature (< 750°C) and fluid-absent conditions plays a key role for the generation of Li-F-rich granites and probably peraluminous RMGPs in general.

Geological setting

The French Massif Central (FMC) exposes a fragment of the inner zone of the European Variscan belt resulting from the continental collision between Laurussia and Gondwana (Faure et al. 2009; Vanderhaeghe et al. 2020). The Variscan evolution in this area features three main stages: (i) early subduction of narrow oceanic basins at 400–360 Ma (Lotout et al. 2020); (ii) crustal thickening and nappe stacking, and (iii) extensional tectonics coeval with a HT regime from ca. 320 to 300 Ma that led to the development of granite–migmatite domes such as the Velay complex in the eastern FMC (Ledru et al. 2001; Bouilhol et al. 2006; Barbey et al. 2015)

(Fig. 1a). Late-orogenic extensional and transcurrent tectonics in the FMC was contemporaneous with peraluminous rare-metal magmatism marked by the emplacement of numerous stocks and dykes of Li-F-rich granites, rhyolites and pegmatites at ca. 310 Ma (Marignac and Cuney 1999; Cuney et al. 2002; Gourcerol et al. 2019) (Fig. 1a). Such occurrences include notably the Beauvoir lepidolite leucogranite, hosted by the zinnwaldite-muscovite granite of Colettes within the Echassières district of the northern FMC, that represents one of the best studied peraluminous rare-metal granites in the world (Cuney et al. 1992; Raimbault et al. 1995; Harlaux et al. 2017; Monnier et al. 2022) (Fig. 1a). A potential 'primitive' or 'less evolved' analogue of Variscan RMGPs is represented by the Li-rich (> 300 ppm) two-mica and topaz-bearing Fabras leucogranite in the southern border of the Velay anatectic dome (Bambier et al. 1985; Montel and Abdelghaffar 1993) (Fig. 1b). The Fabras leucogranite is a small stock (600 x 300m), intruding metatexitic gneisses, that is located close to the border of a Upper Carboniferous to Lower Permian intramontane detrital basin (Montel and Abdelghaffar 1993; Barbey et al. 2015). This leucogranite was possibly sourced from the anatectic rocks occurring in the core of the Velay dome, which exposes deeper structural levels of the Late Carboniferous Variscan crust (Montel et al. 1992; Ledru et al. 2001).

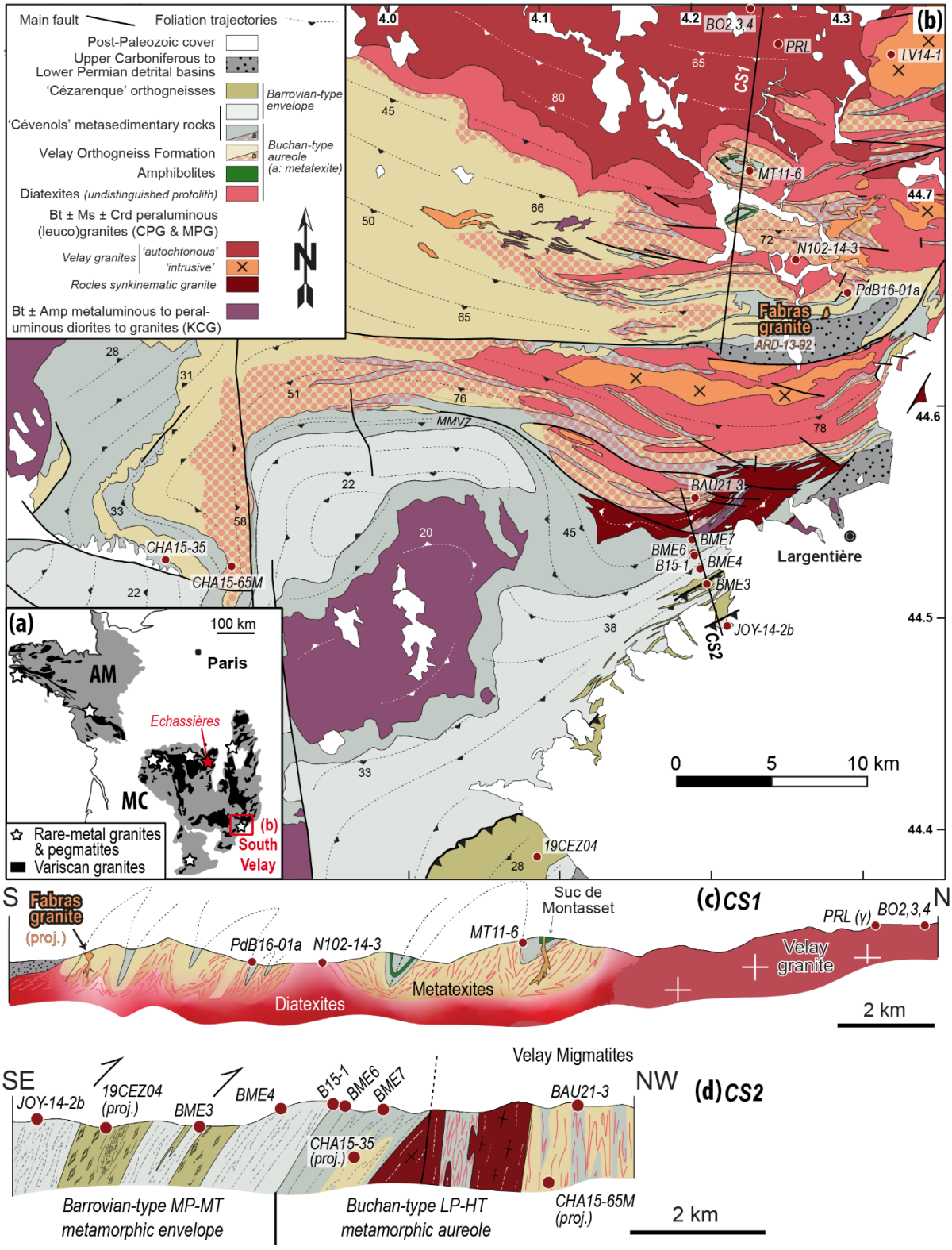

Fig. 1 Geological features of the south Velay area within the French part of the European Variscan belt. **a** Distribution of Variscan granites as well as peraluminous rare-metal granites and pegmatites (Gourcerol et al. 2019) within the Armorican Massif (AM) and the Massif Central (MC). **b-c-d** Simplified geological map and cross sections of the southern part of the Velay dome showing the sample locations. Map redrawn from the regional

geological maps at the 1:50,000 scale. MMVZ: Mylonitic Metamorphic Vellave Zone (from Bouilhol et al. 2006). CPG: cordierite-bearing peraluminous granite. MPG: muscovite-bearing peraluminous granite. KCG: K-feldspar porphyritic calc-alkaline granite. Proj: projected.

Basement rocks within the Southern Velay region consist of: (i) detrital metasedimentary rocks (former pelites, greywackes, sandstones) with Ediacaran maximum depositional ages (590–555 Ma, Couzinié et al. 2019) (Fig. 2a); (ii) Cadomian augen gneisses and leucogneisses, representing former S-type (leuco)granites emplaced at ca. 540 Ma (Couzinié et al. 2017) (Fig. 2b); (iii) Early Ordovician (ca. 490 Ma) felsic metavolcanic rocks ("Cézarenque" orthogneisses) interlayered with post-Ediacaran detrital metasedimentary sequences (Couzinié et al. 2022); and (iv) scarce amphibolites (Ledru et al. 2001). The felsic meta-igneous rocks are peraluminous, and even ferrosilicic for the Early Ordovician ones (Fig. 3a) (Couzinié et al. 2022). Cadomian and Ordovician orthogneisses testify to early partial melting events in the continental crust before the onset of the Variscan orogeny.

Several tectonic-metamorphic events have shaped the terrains exposed in the southern part of the Velay dome. A first event produced a regional schistosity under Barrovian greenschist- to lower amphibolite-facies MP-MT conditions (Toteu and Macaudiere 1984; Arnaud et al. 2004), presumably related to the main crustal thickening stage at ca. 360–340 Ma (Chelle-Michou et al. 2017). The Barrovian metamorphic rocks were reworked by a protracted metamorphic LP–HT event between 320 and 300 Ma (Ledru et al. 2001; Bouilhol et al. 2006; Barbey et al. 2015; Laurent et al. 2017) as evidenced by a typical Buchan-type prograde sequence, which is composed from south to north of biotite–cordierite–andalusite micaschists (Fig. 2c) progressing to biotite-sillimanite ± cordierite gneisses/migmatites (Fig. 2d,e) (Weisbrod 1968; Montel et al. 1992; Bouilhol et al. 2006).

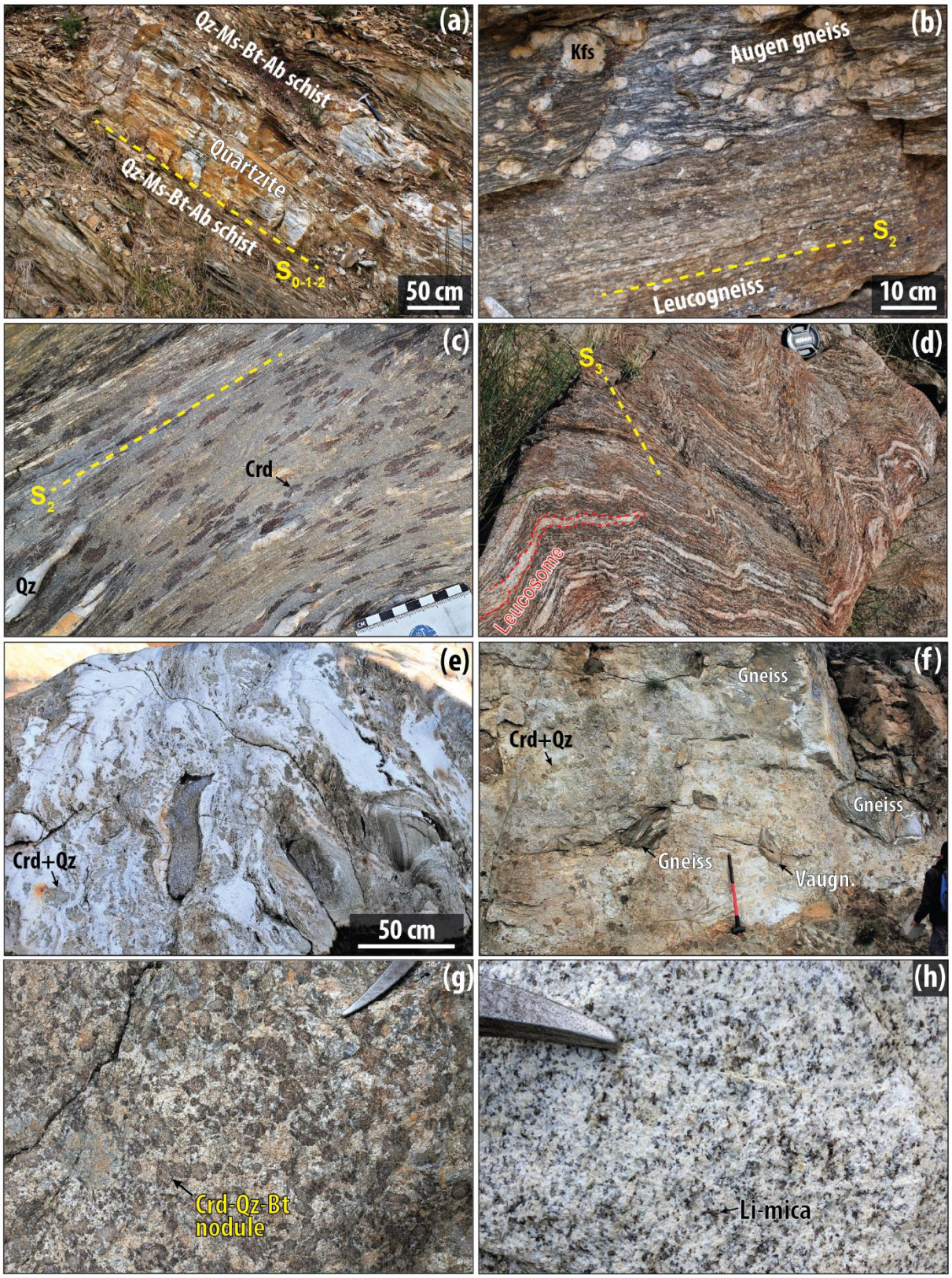

Fig. 2 Field relations of the metamorphic and granitic rocks observed in and near the Velay anatectic dome: **a** Quartz-muscovite-biotite-albite schists with interlayered quartzite (44.5018, 4.1222); **b** Concordant contact between a ca. 540 Ma-old augen gneiss and leucogneiss (44.5630, 3.7602); **c** Cordierite-bearing micaschist

exhibiting regional foliation S2 and cordierite porphyroblasts (44.5369, 4.1969); **d** Metatexitic paragneiss showing S3 folds affecting the metamorphic foliation S2 (44.6254, 4.0157); **e** Diatexite hosting quartz-cordierite aggregates and various metamorphic enclaves (44.7122, 4.2703); **f-g** Heterogeneous Velay granite clattered with various enclaves (**f**: 44.7475, 4.2371) including gneisses and cordierite-quartz-biotite restitic nodules (**g**: 44.79133; 4.25904); **h** Li-mica-topaz-bearing Fabras leucogranite (4.286; 44.645). Abbreviations: Vaugn – vaugnerite; S - foliation. Longitude and latitude coordinates are reported as decimal degrees.

In the migmatitic zone, metatexites (Fig. 2d) are Bt-rich, Ms-free and locally Crd-bearing (mineral abbreviations after Whitney and Evans 2010) indicating fluid-present melting conditions at 650-720°C and 3-5 kbar (Montel et al. 1992; Barbey et al. 2015; Couzinié et al. 2021). Towards the north, the progressive development of Crd and/or Grt-bearing diatexites (Fig. 2e) is attributed to a major crustal melting event under static conditions (Ledru et al. 2001) by massive Bt breakdown around 800°C at 3–4 kbar (Montel et al. 1992; Barbey et al. 2015). Diatexites grade more or less progressively to the heterogeneous "autochthonous" peraluminous Velay granite that is Bt- and/or Crd-bearing, and contains numerous and various enclaves (Fig. 2f,g) (Williamson et al. 1997; Ledru et al. 2001; Villaros et al. 2018). In addition to the main Velay granite, other smaller granitic intrusions were emplaced at different crustal levels throughout the tectonic-metamorphic evolution of the dome, crosscutting the pre-existing metamorphic rocks, the migmatites, and locally the Velay granite. They belong to two main groups: (i) older Kfs porphyritic, locally amphibole-bearing, metaluminous to slightly peraluminous calc-alkaline granitoids (KCG of Barbarin 1999) associated to mantle-derived potassic diorites ("vaugnerites"); and (ii) late Crd- or Ms-bearing peraluminous granites and porphyries (CPG and MPG) (Fig. 3a) (Montel and Abdelghaffar 1993; Barbey et al. 2015; Laurent et al. 2017; Moyen et al. 2017; Villaros et al. 2018). The Fabras topaz and Li-mica-bearing leucogranite belongs to this second group (Figs. 2h and 3a).

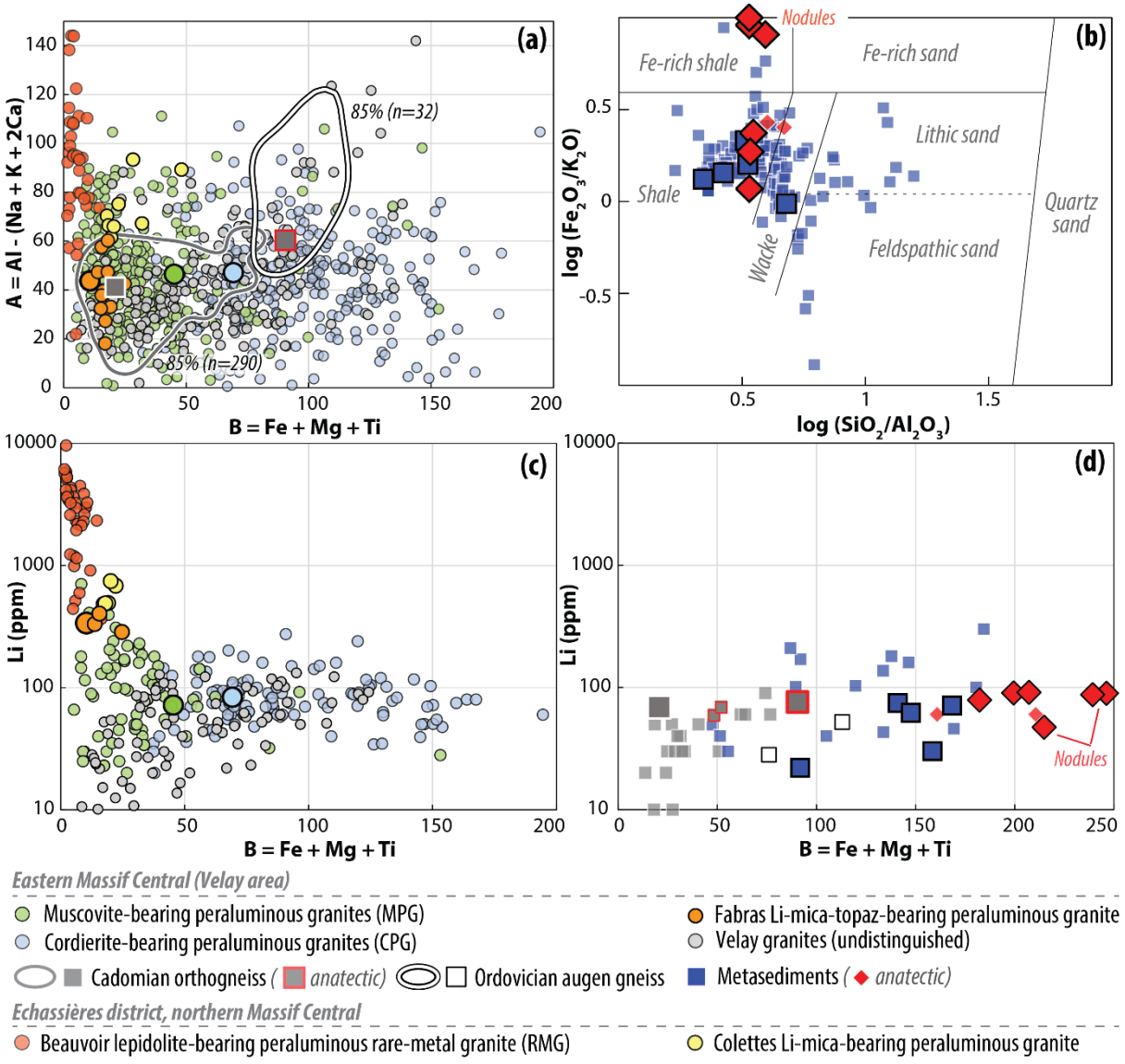

Fig. 3 Whole-rock compositions of peraluminous granites, metasedimentary rocks and orthogneisses from the Velay area and comparison with literature data for granites from the French Massif Central (see Online Resource 2 as well as Moyen et al. 2017, Couzinié et al. 2017, 2022, Raimbault et al. 1995 and Harlaux 2016 for the full dataset). **a** Peraluminous index (A = Al – [Na + K + 2 Ca]) versus differentiation index (B = Fe +Mg + Ti) diagram (Debon and Le Fort 1988) for orthogneisses (shown as fields representing 85% of the samples) and granites. **b** Classification diagram of Herron (1988) for metasedimentary rock samples. **c** and **d** Li concentrations versus B parameter diagram for granites in **c** as well as for potential source rocks including orthogneisses and metasedimentary rocks in **d.** Symbols with larger sizes represent the samples investigated in this study for silicate mineral compositions. Restitic nodules compositions were calculated based on point counting and mineral compositions.

Methods

Whole-rock geochemical analyses were performed at the SARM (CRPG-CNRS, Vandoeuvre-lès-Nancy, France). Mineral backscattered electron (BSE) imaging and micro-XRF chemical mapping as well as *in situ* geochemical analyses were performed on thick and thin sections at the GeoRessources laboratory of the University of Lorraine (Nancy, France). Mineral compositions were determined using electron microprobe analyses (EMPA) and laser ablation-inductively coupled plasma-mass spectrometry (LA-ICP-MS). Additional analytical details, along with data, are provided in Online Resources 1 and 2.

Phase equilibrium modeling was undertaken using the software Perple_X (version 6.9.1, Connolly 2009) in the system (Na$_2$O–CaO–)K$_2$O–FeO–MgO–Al$_2$O$_3$–SiO$_2$–H$_2$O–TiO$_2$, i.e., (NC)KFMASHT. We selected the thermodynamic data file hp62 and the a–x models of White et al. (2014) for garnet, orthopyroxene, cordierite, ilmenite, biotite, staurolite, white mica and melt, and Fuhrman and Lindsley (1988) for feldspar. Bulk compositions used in the modeling are provided in Online resource 3 (Table S1).

Sample petrology and P–T conditions of equilibration

Subsolidus metasedimentary rocks

We investigated a total of nineteen rock samples collected across the study area (Fig. 1b) for which GPS coordinates and hand sample photographs are provided in Online resources 2 and 3 (Fig. S1), respectively. Five samples correspond to pre-Silurian subsolidus metasedimentary rocks from the metamorphic envelope of the Velay dome (BME4; BME6; BME7; JOY14-2b; B15-1) (Fig. 2a,c). Those rocks have mineral assemblages of Qz-Ms ± Bt ± Grt ± Chl ± Ab with Crd-And poikiloblasts developed in the deepest parts of the section (BME6 and BME7). Most samples show typical shale/pelite compositions, except for sample B15-1 that is akin to graywackes (Fig. 3b). Subsolidus metasedimentary rocks have bulk Li and F

concentrations of 20-75 ppm and 0.07-0.09 wt%, respectively (Fig. 3d). Available P–T estimates point to equilibration temperatures in the range 500–550°C for pressures of 3-5 kbar (Bouilhol et al. 2006 and references therein). Consistently, Ti-in-biotite geothermometry (using the calibrations of Henry et al. 2005 and Wu and Chen 2015) applied to our samples yields temperatures between 500 and 650°C (Online Resource 2).

Suprasolidus metasedimentary rocks

Eight suprasolidus metasedimentary rock samples were collected from the migmatitic domain of the Velay dome: three metatexitic paragneisses (MT11-6; BAU21-3a; BAU21-3b), a fine-grained gneiss resister (PdB16-01a), a diatexite (N102-14-3), and three, about 3 cm large, restitic nodules (B02; B03; B04) collected from a very heterogeneous portion of the Velay granite scattered with up to ~2 m large migmatitic enclaves (Fig. 2d,e,f,g). Anatectic metasedimentary rocks, except restitic nodules, show a shale composition similar to most subsolidus metasedimentary rock samples (Fig. 3b) with comparable whole-rock Li contents (60-120 ppm) but higher F (0.15-0.18 wt%) concentrations (Fig. 3d). Based on point counting and mineral composition analyses, the restitic nodules (enriched in Fe) have similar bulk Li concentrations (50-90 ppm) and relatively low bulk F contents (0.04-0.05 wt%) (Fig. 3d).

The metatexitic paragneisses contain tonalitic leucosomes along with Bt-Crd ± Sil ± Grt ± Ap ± Fe-Ti oxides melanosomes (Fig. 4a), and K-feldspar is additionally present in BAU21-3a melanosome. Metatexitic paragneisses show conspicuous biotite-breakdown textures (Fig 4b,c) which are lacking in the Bt-Pl-Qz gneiss PdB16-01a. Muscovite is present in the subsolidus metasedimentary rock samples but absent in the metatexites, suggesting it was fully consumed at lower temperature (≤ ~675°C, ≤ 5.5 kbar) during subsolidus or suprasolidus prograde reactions (Ms + Qz ± Pl = Sil ± melt ± H_2O ± Kfs), depending on pressure and protolith compositions (Online resource 3, Fig. S2). The extensive preservation of biotite and sillimanite together with the general lack of K-feldspar as a reaction product suggest that melting was fluid-

assisted (Weber and Barbey 1986; Montel et al. 1992) and that cordierite formed through the reaction Bt + Sil + Qz + H_2O = Crd ± Grt + melt (Yardley and Barber 1991). Sample N102-14-3 is a diatexite with a melanosome comprising biotite with corroded edges, quartz and poikilitic cordierite as well as accessory apatite and Fe-Ti oxides. The leucosome is primarily composed of quartz, plagioclase, subordinate K-feldspar, biotite and apatite.

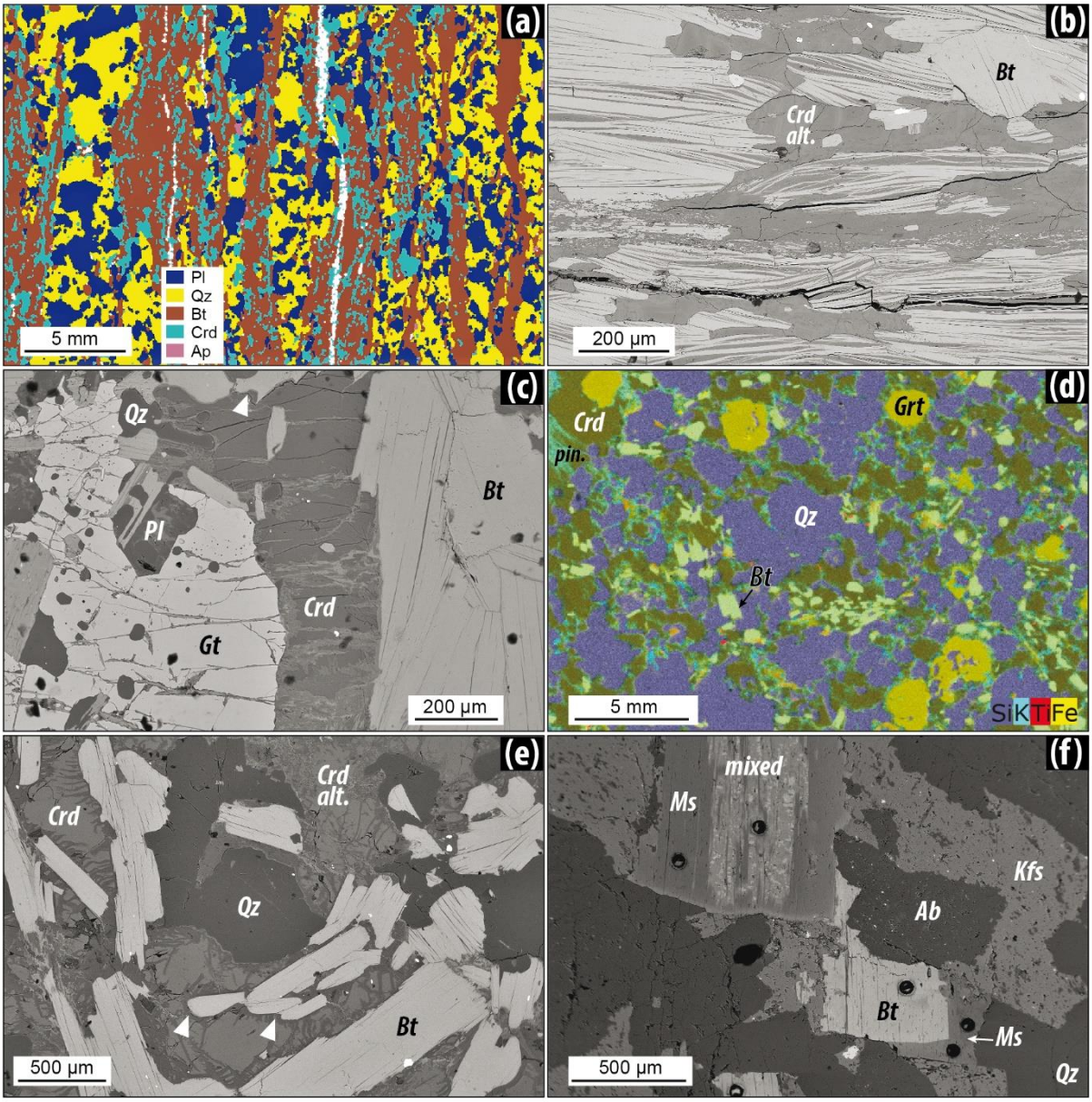

Fig. 4 Petrological features of the studied samples from the Velay anatectic dome. **a** Mineral distribution map of metatexitic paragneiss sample MT11-6, determined by micro-XRF imaging, showing biotite-bearing tonalitic leucosome and intricate biotite-cordierite association in the melanosome; **b** Cordierite (altered to pinite) replacing

biotite in the melanosome of metatexite MT11-6; **c** Suprasolidus fabric of metatexite BAU21-3b with cordierite rimming garnet in contact with corroded biotite (triangle tip) and lobate quartz; **d** Micro-XRF map of restitic nodule sample BO3 showing the intricate cordierite-quartz-biotite association; **e** Suprasolidus fabric in nodule sample BO2 with corroded biotite (triangle tips) replaced by cordierite and lobate quartz; **f** Li-rich biotite (Li-siderophyllite) and Fe-rich muscovite in the Fabras topaz-bearing leucogranite ARD13-92. Mixed zone corresponds to fine-grained assemblage of co-crystallized dioactahedral and trioctahedral micas.

The restitic metasedimentary nodules are embedded in a granitic matrix with sharp contacts (Fig. 2g). They are equivalent to sample B8-A described by Montel et al. (1992). The nodules are primarily composed of roughly 50 vol% Crd, 35 vol% Qz, 10 vol% Bt and 5 vol% Grt (Fig. 4d), along with accessory ilmenite. Garnet is lacking in sample BO4 which contains sillimanite included in biotite. Lobate shapes of Crd-Bt and Crd-Qz contacts, the presence of films of Crd wetting quartz junctions (Fig. 4d,e) collectively support equilibrium with a melt. According to Barbey et al. (1999), the Crd-Qz assemblages were produced upon peritectic reactions of the form Bt + melt = Crd + melt in a magma experiencing decompression. The reaction involved feldspar and sillimanite consumption, when present, and the formation of excess quartz. The nodules are thus interpreted as clusters of restitic minerals (Bt, Grt and Sil) having reacted with their host liquid upon ascent (Montel et al. 1992).

The results of conventional thermobarometry and pseudosection calculations (Online Resource 3, Figs. S2 and S3) performed on the investigated anatectic samples are summarized in Table 1 and are consistent with those obtained by Montel et al. (1992). Migmatites and restitic nodules were equilibrated at mid-crustal pressures of 4–5 kbar and temperatures of 700–830°C with a progressive increase of peak temperatures from metatexites through diatexites to restitic nodules as also recorded by Ti-in-biotite thermometry (Table 1).

Table 1 Summary of P–T estimates obtained for the migmatites investigated in this study.

Sample	Ti-in-Bt (H05)	Ti-in-Bt ; *4.5±1.0 kbar* (W15)	Na-in-Crd (T18); *GASP (H01)*	Grt-Bt (H00); *GASP (H01)*	Grt-Crd (B93); *GASP (H01)*	Pseudosection analysis
PdB16-01a	699±22°C; n=16	647±53°C; n=16	-	-	-	-
MT11-6	704±29°C; n=37	669±58°C; n=37	-	-	-	700-770°C *< 4.6 kbar*
BAU21-3a	695±25°C; n=40	647±51°C; n=40	-	-	-	-
BAU21-3b	711±50°C; n=27	689±61°C; N=27	-	736°C *5.4 kbar*	-	700-780°C *> 5 kbar*
N102-14-3	717±7°C; n=15	711±22°C; n=15	-	-	-	690-780°C *< 4.5 kbar*
BO2	732±23°C; n=30	747±66°C; n=30	760±20°C; n=12 *> 4.4 kbar*	739°C *> 4.2 kbar*	753°C *> 4.3*	790-835°C *4-5 kbar*
BO3	736±20°C; n=18	744±42°C; n=18	761±19; n=17 *> 4.7 kbar*	723°C *> 4 kbar*	755°C *> 4.5 kbar*	790-835°C *4-5 kbar*
BO4	733±26°C; n=19	727±51°C; n=18	758±28°C; n=15 -	-	-	750-820°C *4-5 kbar*

H05 and W15 refer to the Ti-in-biotite thermometers of Henry et al. (2005) and Wu and Chen (2015), respectively. The italic values represent pressures calculated via the GASP barometer (Holdaway 2001) at temperatures obtained by Na-in-cordierite (Tropper et al. 2018), Grt-Bt (Holdaway 2000) and Grt-Crd (Bhattacharya 1993) thermometers. Uncertainties are two standard deviations. GASP barometry along with Grt-Bt and Grt-Crd thermometry relied on average mineral compositions calculated for each sample, as all minerals were chemically unzoned. When sillimanite is absent from the mineral assemblage, the calculated value represents a minimal pressure.

Orthogneisses

Three samples of peraluminous Qz-Pl-Kfs-Ms-Bt meta-igneous rocks collected within the Velay dome (CHA15-65M) and its immediate metamorphic envelope (CHA15-35 and 19CEZ04) were investigated. These samples consist of two Cadomian orthogneisses, including one augen gneiss (CHA15-65M; 549 ± 5 Ma, Couzinié et al. 2021) and one equigranular leucocratic gneiss (leucogneiss CHA15-35, Fig. 2b; 544 ± 5 Ma, Couzinié et al. 2021), as well as one Ordovician augen gneiss (19CEZ04, ca. 490-480 Ma, Couzinié et al. 2022). The leucogneiss sample shows a particularly evolved geochemical signature with a marked

depletion in Fe, Mg and Ti (Fig. 3a) and high F concentrations of 0.15 wt% compared to other orthogneisses (F ~0.08 wt%). The orthogneisses have bulk Li contents of 30-80 ppm similar to those of metasedimentary rocks (Fig. 3d).

The Cadomian augen gneiss is metatexitic and consists of Bt-Ms melanosomes interlayered with quartzofeldspathic leucosomes. According to Couzinié et al. (2021), melting would have proceeded via the eutectic melting reaction again under water-fluxed conditions, with preservation of muscovite due to the low melting temperature of 660-730 °C at 3-7 kbar. The two other orthogneiss samples do not show mineralogical and textural evidence of partial melting.

Variscan granites

Three samples representative of the peraluminous Variscan igneous suites were collected: PRL is a typical biotite-cordierite Velay granite (CPG) with Crd-Qz nodular aggregates; LV14-1 is a biotite-muscovite leucogranite (MPG) from the Quatre-Vios massif (“*microgranite de Laviolle”* in Montel and Abdelghaffar 1993; Thierry et al. 2014); and ARD13-92 is a Li-rich two-mica-topaz granite from the Fabras stock (Fig. 2h). The Fabras granite is characterized by low concentrations in Fe, Mg and Ti along with high Li (280-400 ppm) and F (0.4-0.5 wt%) contents compared to most granites from the eastern FMC (avg. Li ≤ 200 ppm; F ≤ 0.2 wt%), including the Velay (PRL) and Quatre-Vios granite samples (Fig. 3a,c). The composition of the Fabras granite is roughly similar to that of the Li-mica-bearing Colettes granite, hosting the Beauvoir peraluminous rare-metal leucogranite in the Echassières district, northern FMC (Figs. 1a and 3a,c). The Fabras and Quatre-Vios granites contain di- and tri-octahedral micas showing intergrowth textures suggesting co-crystallization (Fig. 4f).

Compositions of micas, cordierite and garnet

Major element composition and classification

Micas (muscovite and biotite), garnet and cordierite from ortho- and para-derived metamorphic rocks along with granites from the Velay dome were analyzed to determine their major and trace element compositions, with a focus on F and Li contents. Cordierite has similar Mg# [Mg/(Mg+Fe) – apfu] values between 0.5 and 0.6 in suprasolidus metasedimentary rocks and the cordierite-bearing granite. Cordierite is completely altered to pinite (i.e., a fine-grained assemblage of chlorite and white micas) in subsolidus metasedimentary rocks. Garnet from metasedimentary rocks is chemically homogeneous and has a dominant almandine component ($0.72 \leq X_{Alm} \leq 0.78$).

Tri- and di-octahedral micas from most samples globally show Fe-biotite ($0.30 \leq Mg\# \leq 0.45$) and muscovite compositions (see classification diagrams in Online Resource 3, Fig. S4). Exceptions comprise the Fabras leucogranite which contains Fe-rich muscovite along with Li-rich trioctahedral micas ($0.10 \leq Mg\# \leq 0.20$), having intermediate compositions between Fe-biotite and zinnwaldite (Li-siderophyllite according to Tischendorf et al. 1997). Moreover, biotite in the Cadomian leucogneiss is characterized by low Mg# of ~0.1 (siderophyllite of Tischendorf et al. 1997) whereas biotite from the Ordovician orthogneiss is slightly more magnesian compared to other samples (Mg# ~0.50). Dioctahedral micas in B15-1 metagraywacke are more heterogeneous in terms of composition than that from metapelites and reach higher Fe concentrations.

Mineral/mineral element partitioning

Partitioning data of Li and F between coexisting micas, garnet and cordierite for rocks from the Velay dome are shown in Figure 5 and Table 2. No significant compositional differences are observed within migmatites between micas from melanosomes and that from respective leucosomes, indicating that leucosome micas could be restitic. This is true for Li and F, and also for other elements, thus leucosomes and melanosomes are not distinguished in the following. In all rock types, biotite is systematically enriched in Li and F compared to

muscovite, by factors of ~2 to 10 and ~2 to 5, respectively (Fig. 5a,b). A similar behavior is observed for Cs, Nb and Ta, whereas the opposite is true for Be, Sn and W that preferentially partition in muscovite relatively to biotite (Online Resource 3, Fig. S5, Table S2).

Biotite has 6 to 15 times more Li than garnet in metasedimentary rocks (Fig. 5c). In contrast, the Li concentration of cordierite is about 2 to 3 times higher than that of coexisting biotite (Fig. 5d). We note that Be is strongly enriched in cordierite compared to biotite (factor of ~100 to 400) and Cs shows biotite over cordierite content ratios ($Kd^{Bt/Crd}$) between ~1 and 5 (Online Resource 3, Fig. S6, Table S2). Cordierite and garnet do not incorporate significant amounts of other rare-metals and halogens. Mineral/mineral element partitioning data obtained for rocks from the Velay dome are consistent with those calculated using published data for igneous and metamorphic rocks from other areas (Fig. 5).

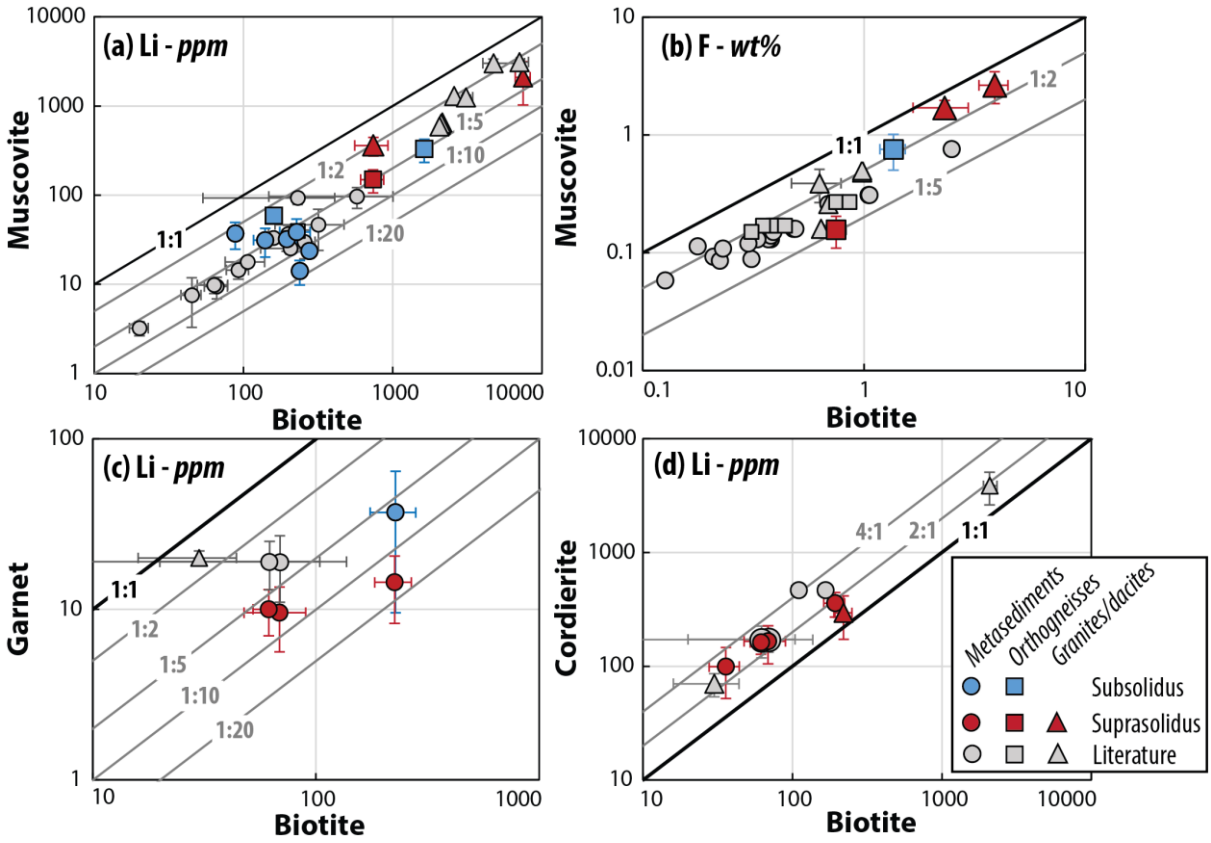

Fig. 5 Mean Li and F concentrations of coexisting biotite, muscovite **a-b**, garnet **c** and cordierite **d** for para- and ortho-derived metamorphic rocks, migmatites and granites from the Velay dome. Literature data for granites,

dacites, gneisses and metasedimentary rocks (Bea et al. 1994; Neves 1997; Acosta-Vigil et al. 2010; Simons et al. 2017; Zhou et al. 2021; Kunz et al. 2022; Sallet et al. 2023) are shown for comparison. Error bars show two standard deviations.

The affinity of Be for cordierite results from its structure, since cordierite is isostructural with beryl. Beryllium is incorporated in tetrahedra, replacing Al through the coupled exchange $Be^{2+} + Si^{4+} \rightarrow 2\ Al^{3+}$, or alternatively by adding a monovalent cation in the central channel, such as K^+ or Na^+ (Franz and Morteani 2002; Bertoldi et al. 2004). Lithium is accommodated in the octahedral site, replacing Fe and Mg, again with some charge compensation in other sites (Gordillo et al. 1985; Bertoldi et al. 2004).

Table 2 Mineral-mineral partitioning data of Li and F for Velay samples.

Sample	Li									F		
	$Kd^{Bt/Ms}$	*2σ (+)*	*2σ (-)*	$Kd^{Crd/Bt}$	*2σ (+)*	*2σ (-)*	$Kd^{Bt/Grt}$	*2σ (+)*	*2σ (-)*	$Kd^{Bt/Ms}$	*2σ (+)*	*2σ (-)*
Subsolidus metasedimentary rock												
BME4	4.5	3.6	1.7	-	-	-	-	-	-	-	-	-
JOY14-2b	5.9	6.2	2.7	-	-	-	6.2	23.2	3.4	-	-	-
B15-1	2.4	1.5	0.8	-	-	-	-	-	-	-	-	-
BME6	16.9	9.3	5.0	-	-	-	-	-	-	-	-	-
BME7	11.7	3.7	2.6	-	-	-	-	-	-	-	-	-
Subsolidus Ordovician orthogneiss												
19CEZ04	2.7	0.9	0.6	-	-	-	-	-	-	-	-	-
Subsolidus Cadomian orthogneiss												
CHA15-35	5.0	2.8	1.5	-	-	-	-	-	-	1.8	1.3	0.6
Suprasolidus metasedimentary rock												
BAU21-3b	-	-	-	-	-	-	15.7	16.7	6.7	-	-	-
N102-14-3	-	-	-	1.8	0.9	0.6	-	-	-	-	-	-
B02	-	-	-	2.4	2.4	1.2	7.2	8.8	3.7	-	-	-
B04	-	-	-	2.8	2.5	1.6	-	-	-	-	-	-
B03	-	-	-	2.6	1.1	0.8	6.1	4.0	2.1	-	-	-
Suprasolidus Cadomian orthogneiss												
CHA15-65M	5.0	3.3	1.8	-	-	-	-	-	-	4.8	2.8	1.5
Cordierite-bearing granite												
PRL	-	-	-	1.3	0.9	0.6	-	-	-	-	-	-
Muscovite-bearing granite												
LV14-01	2.1	1.3	0.8	-	-	-	-	-	-	1.4	0.7	0.5
Li-mica-bearing granite												
ARD13-92a	3.6	4.5	1.5	-	-	-	-	-	-	1.5	1.0	0.5

Lithium and halogen compositional evolutions as a function of temperature and protolith

We here document the behavior of Li and F during prograde regional metamorphism and crustal melting using minerals that are stable both at sub- and supra-solidus conditions namely biotite, cordierite and garnet (Fig. 6). The composition of muscovite is not described in the following as it does not occur in the investigated anatectic metamorphic rock samples, except for one

augen gneiss. The Li concentrations of biotite from subsolidus metasedimentary rocks are similar to those from migmatitic paragneisses ranging from ~90 to 280 ppm (Fig. 6a). However, a significant drop of biotite Li concentrations down to 35-70 ppm is observed above ~750°C for high-temperature restitic nodules. The Li content of cordierite mimics that of biotite and decreases with temperature from migmatites (~360 ppm) to restitic nodules (~100-160 ppm). Garnet has a higher Li content (~40 ppm) in subsolidus metasedimentary rocks compared to suprasolidus equivalents (~10-15 ppm). Fluorine shows a distinct behavior than Li as the concentration in biotite, ranging from 0.15 to 0.55 wt%, is roughly constant or tends to increase with temperature (Fig. 6b). Beryllium (~0.01-0.70 ppm), W (~2-9 ppm) and Cs (~20-50 ppm) show a behavior comparable to Li as their concentrations decrease above ~750°C in biotite from anatectic metasedimentary rocks (Online Resource 3, Fig. S7). However, Sn (~9-20 ppm), Nb (~30-120 ppm) and Ta (~2-8 ppm) behave like F as their concentrations in biotite slightly increase or remain constant with increasing temperature.

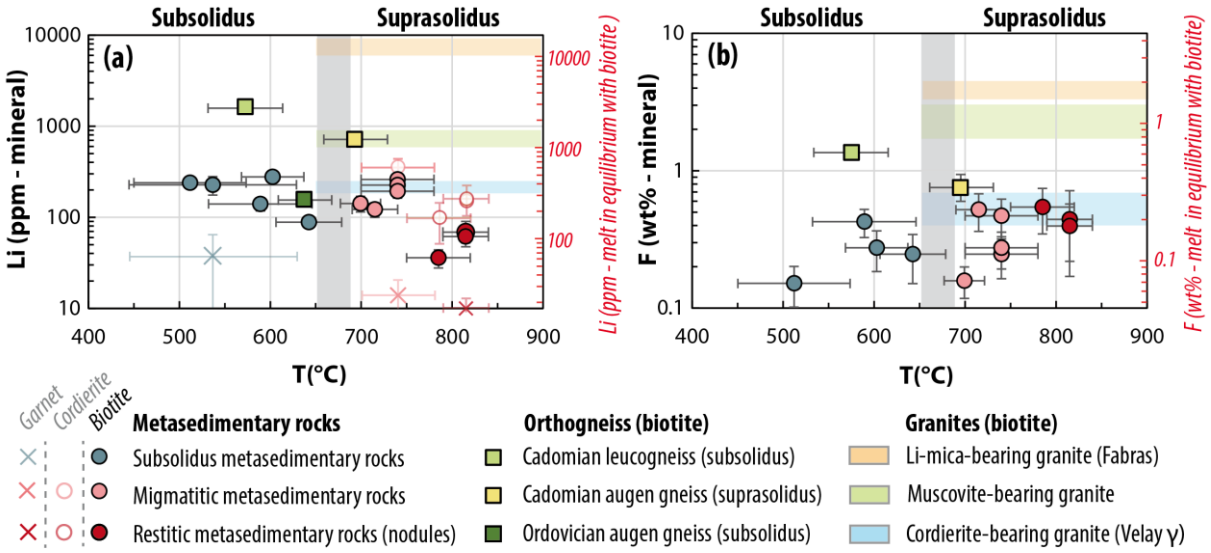

Fig. 6 Evolution of the average **a** Li and **b** F compositions of biotite, cordierite and garnet, with errors at 2 sigma deviation (SD), as a function of peak temperatures for para- and ortho-derived metamorphic rocks from the Velay dome. The range of Li-F contents in igneous biotite from Variscan granites is shown for comparison (colored fields). Temperatures were calculated based on the Ti-in-biotite geothermometer (Henry et al. 2005) for subsolidus metamorphic rocks and errors bars show 2SD. Mean temperatures and associated uncertainties for suprasolidus

metamorphic rocks were estimated based on pseudosection analyses (Table 1), except for one sample (PdB16-01), for which temperature was determined by Ti-in-biotite thermometry. The grey field corresponds to the temperature range of muscovite dehydration for metasedimentary rocks. The red axes on the right side of each diagram correspond to the composition of the melt in equilibrium with biotite for suprasolidus rocks calculated using preferred $Kd^{biotite/melt}$ values of 0.55 (Li) and 2.25 (F) of Villaros and Pichavant (2019).

The Li-F compositions of biotite in para-derived migmatites are similar to that of biotite from the cordierite-bearing granite (Li ~220 ppm, F ~0.55 wt%). Such values are significantly lower than that of trioctahedral micas from muscovite-bearing (Li ~740 ppm, F ~2.30 wt%) and Li-mica-bearing (Li ~7,500 ppm, F ~3.90 wt%) granites (Fig. 6). The Li content (~160 ppm) of biotite in the Ordovician orthogneiss is comparable to that from metasedimentary rocks. However, biotite from Cadomian orthogneisses (especially the leucogneiss) reaches distinctly higher Li (740-1,630 ppm) and F (0.75-1.40 wt%) concentrations (Fig. 6). Biotite from Cadomian orthogneisses is also enriched in other rare-metals such as Cs (80-230 ppm), W (5-11 ppm), Sn (40-80 ppm), Nb (100-260 ppm) and Ta (10-30 ppm). Those concentrations are similar to or below that of trioctahedral micas from the Li-mica-bearing Fabras granite and above that of the cordierite-bearing Velay granite (Online Resource 3, Fig. S7).

Geochemical modeling of Li-F enrichment in crustal melts

In this section, we explore the behavior of F and Li during crustal melting using geochemical modeling. We aim at unraveling the respective role of different key parameters which include temperature, pressure, melt extraction (restite melting scenario), protolith composition and H_2O activity on the F-Li enrichment of anatectic silicate melts.

Li partitioning in cordierite

As shown by our mineral/mineral partitioning data (Fig. 5, Table 2), Li is readily incorporated in cordierite relatively to biotite whereas cordierite does not incorporate substantial amounts of F. The mean $Kd_{Li}^{Crd/Bt}$ values range from 1.8 to 2.8 in anatectic metasedimentary rocks and is

of 1.3 in the cordierite-bearing granite. As Li is mildly incompatible to compatible in biotite ($0.4 \leq Kd^{Bt/melt} \leq 1.7$; Villaros and Pichavant 2019), $Kd_{Li}^{Crd/melt}$ must be above 1. Our data are not consistent with the experimental results of Evensen and London (2003) which suggest that Li preferentially partitions into biotite over cordierite, and that Li is incompatible in the latter. However, our data are in agreement with previous data on natural rocks which show $Kd^{Crd/Bt}$ values from ~2 to 4, including felsic volcanic rocks not susceptible to retrograde re-equilibration and peraluminous granites that host cordierite with up to 3,000 ppm Li (Fig. 5d) (Gordillo et al. 1985; Bea et al. 1994; Černý et al. 1997; Acosta-Vigil et al. 2010; Alasino et al. 2010; Simons et al. 2017). Actually, the positive Na-Li correlation in cordierite observed from our dataset is consistent with the classical substitution scheme $(Na^{+}_{Channel} + Li^{+}_{Oct}) \rightarrow (Mg^{2+}, Fe^{2+})_{Oct}$ (Online Resource 3, Fig. S8). Therefore, the following geochemical modeling will rely on natural cordierite/mineral partitioning data.

Modeling approach

Following the methodology of Mohammadi et al. (2016) and Janoušek and Moyen (2020), the Li-F content of modeled melts and solid residues were estimated along two P–T paths mimicking different melting scenarios (Fig. 7). Paths MP and LP correspond to isobaric heating from 650 to 850°C at 7 and 4.5 kbar, respectively. The phase proportions were obtained via PerpleX. The set of partition coefficients (Table 3) was built on the experimental data compiled by Villaros and Pichavant (2019) and on $Kd^{biotite/mineral}$ values from the Velay samples. The compositions of melts and residues were calculated using the batch melting equation, as fractional melting is probably not realistic considering the relatively high viscosity of granitic magmas.

Metasedimentary rock melting modeling was done using as a protolith the subsolidus metapelitic sample BME7 (Fig. 7a), with 70 ppm Li and 0.081 wt% F. H_2O was settled at 1.8

wt%, based on the modal abundance of micas in the rock and considering 5 wt% H_2O in micas, to firstly reproduce "fluid-absent" melting conditions (Online Resource 3, Table S1). Re-melting of a biotite-rich residue left after melt extraction from a BME7-like source was also simulated at 7 kbar to test the restite melting scenario (Fig. 7b) and more details on the modeling approach are given below. Orthogneiss partial melting was modeled at 7 kbar using the CHA15-35 leucogneiss as a starting composition (Fig. 7c). The H_2O content of the leucogneiss was set to a value of 0.68 wt% corresponding to melt saturation at the 7 kbar solidus (based on a T-X(H_2O) section, Online Resource 3, Fig. S9), a value close to the LOI. The initial bulk Li-F concentrations of the orthogneiss was set to 70 ppm Li and 0.081 wt% F (i.e., the composition of BME7 metapelite) in order to only evaluate the effect of protolith mineralogy on melt compositions.

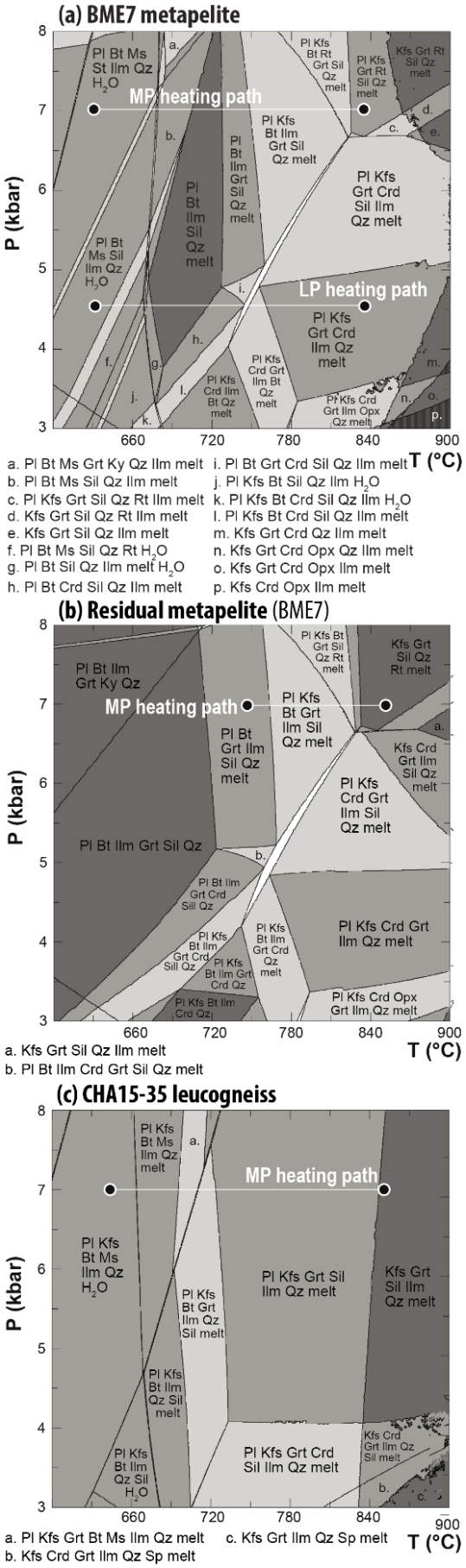

Fig. 7 Pseudosections for a Velay metapelite (BME7, **a**) and calculated residual equivalent **b**, as well as for a Cadomian leucogneiss (CHA15-35, **c**)**.** The medium pressure (MP) and low pressure (LP) paths, along which phase proportions and Li-F melt/residue partitioning were calculated, are indicated. Pseudosection **b** represents the residual metapelite, after the extraction of 25 vol% melt from BME7, that was calculated in order to model restite melting.

Table 3 Partitioning data for Li and F used for partial melting models.

	Li			F		
	Min	Pref	*Max*	*Min*	Pref	*Max*
Kd $^{Bt/melt}$	0.41 [a]	0.55 [a]	1.67 [a]	1.56 [a]	2.25 [a]	4.00 [a]
Kd $^{Crd/Bt}$	-	2.00 [b]	-	-	-	-
Kd $^{Bt/Grt}$	-	6.00 [b]	-	-	-	-
Kd $^{Bt/Ms}$	-	5.00 [b]	-	-	-	-
Kd $^{Crd/melt}$	0.82 [c]	1.10 [c]	3.34 [c]	0.01 [d]	0.01 [d]	0.01 [d]
Kd $^{Grt/melt}$	0.07 [c]	0.09 [c]	0.28 [c]	0.01 [d]	0.01 [d]	0.01 [d]
Kd $^{Ms/melt}$	0.08 [c]	0.11 [c]	0.33 [c]	0.94 [a]	1.00 [a]	1.92 [a]

Pref: preferred; a: experimental Kd data compiled by Villaros and Pichavant (2019); b: values based on Velay rock samples (this study); c: values calculated using experimental Kd Bt/melt and Velay rock Kd mineral/mineral values; d: assumed values. The Kd of all other minerals was fixed to 0.01.

Metapelite melting model and the impact of pressure and cordierite crystallization upon Li enrichment in silicate melts

The compatibility of Li in cordierite inhibits Li enrichment in the melt during the low-pressure dehydration melting reaction of biotite below ~5-6 kbar (Bt + Qz + Pl = melt + Kfs + Crd), contrary to garnet (Bt + Qz + Pl = melt + Kfs + Grt) which does not incorporate significant amounts of Li. The modeled Li content of liquids produced during metapelite anatexis are shown in Figure 8. At both low (Fig. 8a) and medium (Fig. 8b) pressure (i.e., within and outside the stability field of cordierite, respectively), the melt is enriched in Li relatively to the residue and the protolith. With increasing temperature, the Li concentration in the melt decreases as the melt proportion increases (dilution effect). The muscovite-out reaction occurs at low temperature around 670°C for the LP path, explaining its absence in the investigated anatectic metasedimentary rocks having minimum peak temperatures around 700°C (Fig. 6). At 7 kbar, this reaction occurs at slightly higher temperature around 700˚C. Similarly, the biotite-out reaction occurs at lower temperature along the LP path (~750˚C) than along the MP path (~825˚C). The first significant amounts of melts (~10 wt%) produced below 700°C have similar Li concentrations around 250-300 ppm at low and medium pressure. However, above 700°C, peritectic cordierite crystallization along the LP path induces a stronger decrease of melt Li concentrations relatively to the melt produced at higher pressure. At ~750°C, the difference between LP (~125 ppm) and MP (~250 ppm) melts is maximum and reaches a factor 2.

As cordierite crystallization cannot inhibit F enrichment of the melt, F partitioning during metapelite melting was only modeled at 7 kbar. In contrast to Li (Fig. 9a), the modeled F concentration of the melt remains similar to the protolith (~0.08 wt%) from ~670 to 750°C and then slightly increases up to ~0.10 wt% around 800 °C (Fig. 9b).

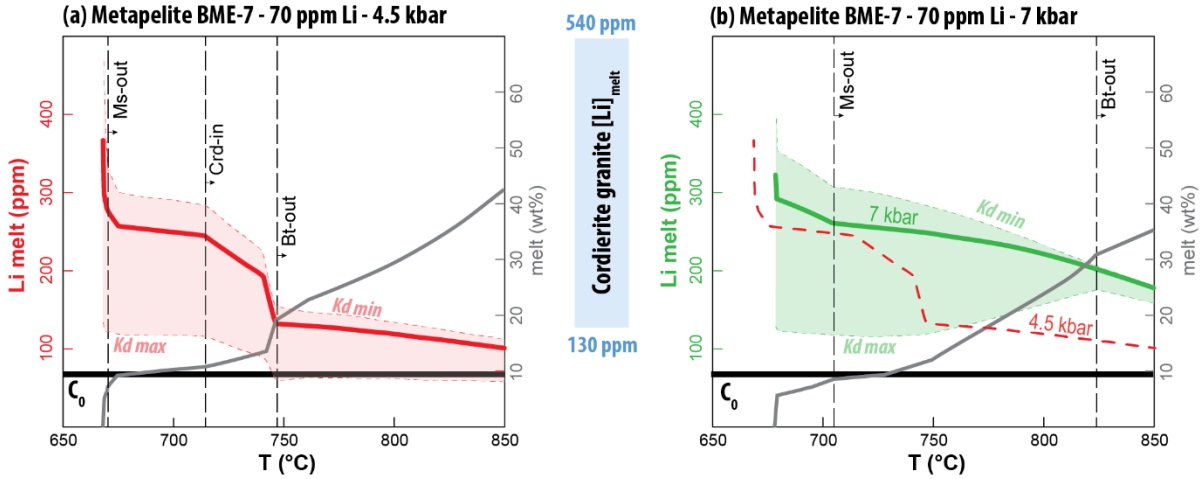

Fig. 8 Lithium concentrations in melt versus temperature diagrams illustrating the results of batch melting modeling for a typical metapelite (BME7) from the Velay dome with H_2O concentration in the protolith settled at 1.8 wt%. Partial melting was simulated at **a** 4.5 kbar and **b** 7 kbar within and outside the stability field of cordierite, respectively. The light-colored fields show deviations related to the use of minimum and maximum $Kd^{biotite/melt}$ values from the literature. Melt amounts are shown as grey curves. The blue field represents the range of Li composition of the melt in equilibrium with the biotite of the cordierite-bearing granite based on maximum and minimum Kd values (Table 3). C_0 represents the initial composition of the metapelite.

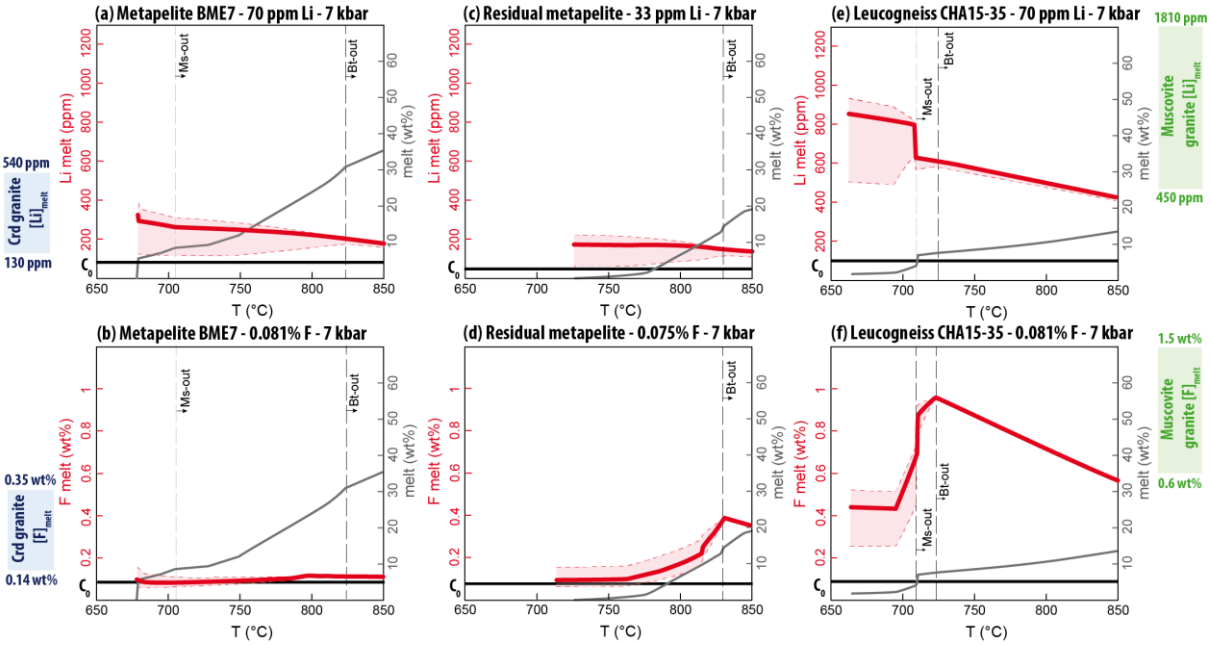

Fig. 9 Lithium and F concentrations in melt versus temperature diagrams comparing results of batch melting modeling for a metapelite (1.8 wt% H_2O) **a-b**, a residual metapelite **c-d**, and a leucogneiss (0.7 wt% H_2O) **e-f** from the Velay dome at 7 kbar. Melt amounts (wt%) are shown as grey curves. Blue and green fields represent the range

of Li and F compositions of melts in equilibrium with the biotite of the cordierite- and muscovite-bearing granites, respectively. C_0 represents the initial composition of the protoliths.

Restitic metapelite melting model

It has been proposed that granitic melts enriched in rare-metals including Li and halogens such as F can be produced by re-melting of a biotite-rich residue (restite) (e.g., Simons et al. 2016; Michaud et al. 2021). To test this hypothesis, we modeled the re-melting of the solid residue left after extraction of ~25 vol% melt at 750°C and 7 kbar from the BME7 metapelite. We considered that 1 mol% melt was retained in the source following Korhonen et al. (2013). The solid residue is composed of Qz + Bt + Pl + Sil + Grt + Ilm (Fig. 7b). The residue contains 0.075 wt% F, but only 33 ppm Li because the Li-rich melt was lost along the prograde path.

Fluid-absent melting of such restitic metapelite between ~750 and 800°C produces a melt with a nearly constant Li concentration of ~175 ppm at 7 kbar, relatively close to that of the fertile metapelite, and slightly decreases down to ~100-150 ppm after biotite exhaustion around 830°C (Fig. 9c). In contrast, the F concentration of the melt produced by restite melting significantly increases with temperature from ~0.1 to 0.4 wt%, and the maximum content is attained at the Bt-out isograd (Fig. 9d). Such F melt composition is higher than that produced during fertile metapelite melting ($\leq$ 0.1 wt%, Fig. 9b).

Orthogneiss melting model

As observed for the metapelite, partial melting of the orthogneiss produces a melt enriched in Li compared to the protolith (and residue), and the Li concentration of the melt decreases with increasing melting degree and temperature (Fig. 9e). However, the Li concentration of the melts produced from the orthogneiss source is significantly higher than that generated from the metapelite source, with a factor of enrichment above 2 (600 ppm versus 250 ppm) at ~710°C (Fig. 9a,e). This is because the orthogneiss protolith has a lower mica proportion than the

metapelite. Therefore, the complete breakdown of muscovite and biotite for the orthogneiss occurs at relatively low temperature of ~730°C and produces ~10 wt% melt enriched in Li. By comparison, biotite-out for the metapelite occurs around 825°C at 7 kbar and can produce up to 35 wt% of melt, but this melt is Li-poor due to dilution. Moreover, the model indicates that a strong enrichment of F up to ~1 wt% occurs in the melt at ~720°C simultaneously with high concentrations of Li (~600 ppm) during orthogneiss melting (Fig. 9f).

Fluid-absent versus water-fluxed melting

The effect of water-fluxed melting versus fluid-absent melting (Figs. 8 and 9) on Li enrichment in anatectic melts is evaluated by increasing the initial bulk H_2O content of metapelitic and orthogneissic protoliths (Fig. 10). For the metapelite BME7, the evolution of Li melt concentrations produced using an initial bulk H_2O content of 1.8 wt%, is compared to that produced using higher bulk H_2O content of 3.0 wt%, a value close to the LOI (Fig. 10a). For the leucogneiss CHA15-35, the bulk water concentration was also increased from 0.7 to 3.0 wt% for sake of comparison (Fig. 10b). The respective pseudosections for both protoliths at higher bulk water contents are provided in Online Resource 3, Fig. S10.

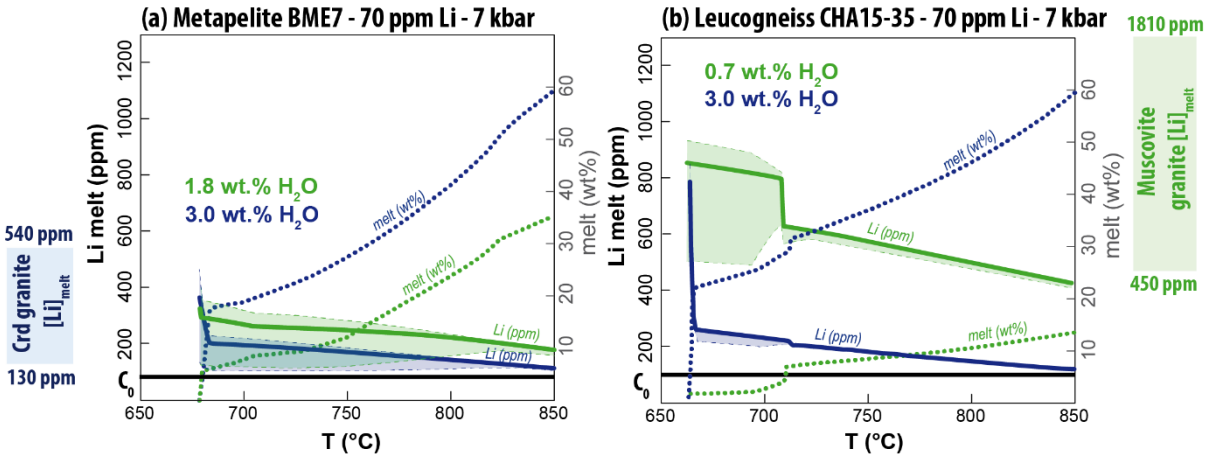

Fig. 10 Lithium concentrations in melt versus temperature diagrams illustrating the effect of increasing whole-rock H_2O concentration of the protolith on batch melting modeling results for a metapelite **a** and leucogneiss **b** from the Velay dome at 7 kbar. The green and blue curves represent Li melt concentration evolutions for low (1.8

wt% in **a**; 0.7 wt% in **b**) and high (3.0 wt%) water contents in each protoliths, respectively. The dashed curves indicate the melt proportion in wt%. The Li and F compositions of melts in equilibrium with the biotite of the cordierite- and muscovite-bearing granites are indicated as fields. C_0 represents the initial composition of the protoliths.

Similarly to the "fluid-absent" melting scenarios, the Li melt concentrations decrease as a function of temperature when more water is added to both protoliths, but concentrations are lower at a given temperature during "water-fluxed" melting. From ~670 to 850°C, the Li melt concentrations produced from the metapelite decrease from ~200 to ~100 ppm at high-water content, whereas concentrations decrease from ~300 to ~175 ppm at low-water content, which corresponds to an enrichment factor of ~1.5-2.0 from "wet" to "damp" conditions (Fig. 10a). The Li concentration gap between melts generated upon "fluid-absent" and "fluid-fluxed" melting conditions is significantly higher for the leucogneiss (factor of ~4, Fig. 10b). In the temperature range of 660 to 850°C, Li melt concentration decreases from ~300 to 100 ppm if 3 wt% H_2O is settled in the protolith, whereas concentrations decrease from ~850 ppm to 400 ppm at "damp" conditions (0.7 wt% H_2O). For both protoliths, the decrease of Li melt concentrations in function of their water content is due to dilution, as adding water to the protolith significantly increases melt proportions. From "damp" to "wet" conditions, maximum melt proportions at 850°C increase from ~35 to 60 wt% and from ~15 to 60 wt% in the case of the metapelite and leucogneiss, respectively. The leucogneisses are indeed more sensitive to this effect because of their "near-eutectic" composition (Couzinié et al. 2021).

Discussion

Biotite compositions as proxies of Li-F enrichment in anatectic silicate melts: comparison with whole-rock data and modeling results

The Li contents of biotite and cordierite from suprasolidus metasedimentary rocks from the Velay anatectic dome decrease by a factor of ~3 above 750°C (Fig. 6a). Based on available

$Kd^{Bt/melt}$ values (Table 3), we calculate that the Li contents of silicate melts in equilibrium with biotite decreased from ~200-400 ppm to 60-100 ppm with the progress of the biotite-breakdown melting reaction from migmatites to restitic nodules (Fig. 6a). In contrast, the F concentrations of biotite from suprasolidus metasedimentary rocks remain constant or tend to increase with temperature; the estimated equilibrium melt F content ranging from ~0.07 to 0.25 wt% (Fig. 6b). The relative melt concentration evolutions of F and Li recorded by biotite are in agreement with the results of "water-fluxed" metapelite melting modeling at 4.5 kbar, i.e., the conditions relevant for the Velay anatectic dome (Fig. 11). This, together with above-solidus Ti-in-biotite temperatures (≥ 700 °C, Table 1, Henry et al. 2005) and uniform biotite-cordierite Li partitioning data (Fig. 5 and Table 2), suggests that the Li-F compositions of minerals were not re-equilibrated at sub-solidus conditions. Biotite compositions are thus good proxies of melt compositional evolutions upon crustal anatexis in the Velay dome.

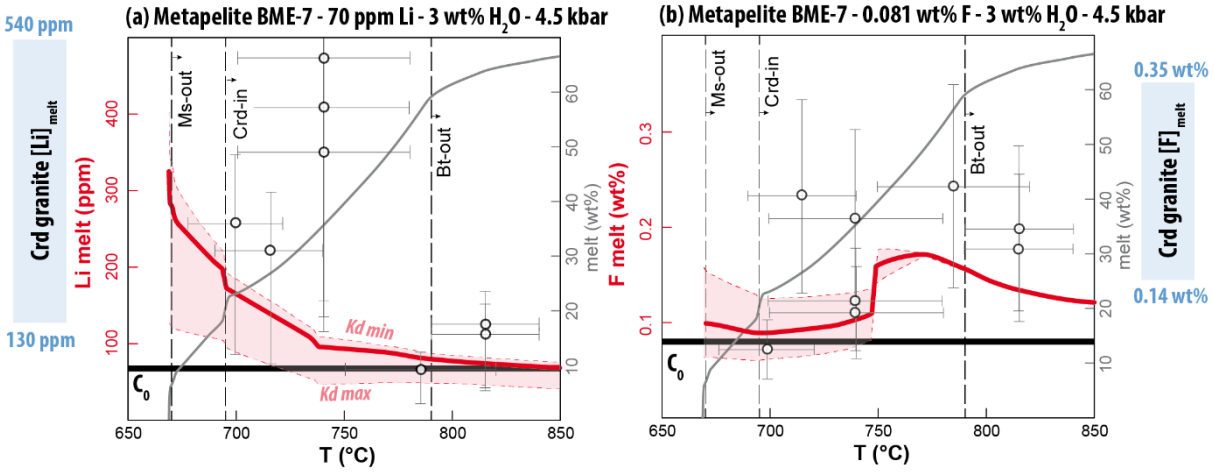

Fig. 11 Lithium **a** and F **b** concentrations in melt versus temperature diagrams illustrating the results of batch melting modeling for the BME7 metapelite at the conditions relevant from the Velay dome (i.e., 4.5 kbar and "wet" conditions with H_2O content in the protolith settled at 3 wt%). The melt concentrations in equilibrium with biotite from anatectic metasedimentary rocks (white points) and cordierite granite (blue field) from the Velay dome, calculated based on preferred, minimum and maximum Kd values (Table 3) are shown for comparison. The grey curves show the melt proportion and C_0 represents the initial composition of the protolith.

Both modeling and biotite compositions support a contrasted behavior of Li and F during partial melting of metapelites. This is true at low pressure < 5 kbar (Fig. 11) but also at higher pressures (Fig. 9a,b). Lithium behaved incompatibly with respect to residual silicate minerals and the Li-richest melts (200-400 ppm) were produced at low temperature ≤ 750°C during muscovite- or incipient biotite-breakdown. In contrast, F behaved more compatibly; F melt concentrations (~0.1-0.2 wt%) remained relatively stable with temperature with a slight concentration increase at T > 750°C. Similar behavior for both Li and F were reported for biotite from sub- to supra-solidus metasedimentary rocks from the Ivrea Zone in the European Alps and the Langtang Himalaya in Nepal (Kunz et al. 2022), as well as for metamorphic rocks from the Rogaland metamorphic aureole in Norway (Finch and Tomkins 2017) (Online Resource 3, Fig. S11).

Whole-rock data alone do not allow to trace with the same accuracy the behavior of both elements upon partial melting, but are complementary to silicate mineral compositions. In the Velay dome, bulk Li contents are roughly similar for para-derived migmatites (60-120 ppm) and restitic nodules (50-90 ppm) due to the abundance of peritectic cordierite in the latter (~50 vol%, Fig. 4d) for which Li is compatible (Fig. 12a). Therefore, calculated melt concentrations in equilibrium with biotite are enriched relative to corresponding bulk migmatites at < 750 °C but melt and whole-rock contents are almost equivalent for restitic nodules at > 750°C (Fig. 12a). Regarding F, whole-rock concentrations decrease significantly from 0.15-0.18 wt% to 0.04-0.05 wt% above 750°C. This is due to the progress of the biotite-breakdown reaction and the absence of other mineral phases incorporating F, such as apatite, in restitic nodules (Fig. 12b). Melt and whole-rock F concentrations are similar at < 750°C but melts are enriched relative to bulk restitic nodules at > 750°C, as F behave more incompatibly at these temperatures. In the Ivrea zone, the whole-rock Li concentrations of metasedimentary rocks decrease with temperature, similarly as biotite Li contents (Bea and Montero 1999; Qiu et al.

2011; Kunz et al. 2022) (Online Resource 2, Fig. S11). Contrary to the Velay area, melt equilibrated with biotite are always enriched in Li relative to whole-rock samples, as cordierite is generally not stable at the melting conditions of the Ivrea zone (> 5 kbar).

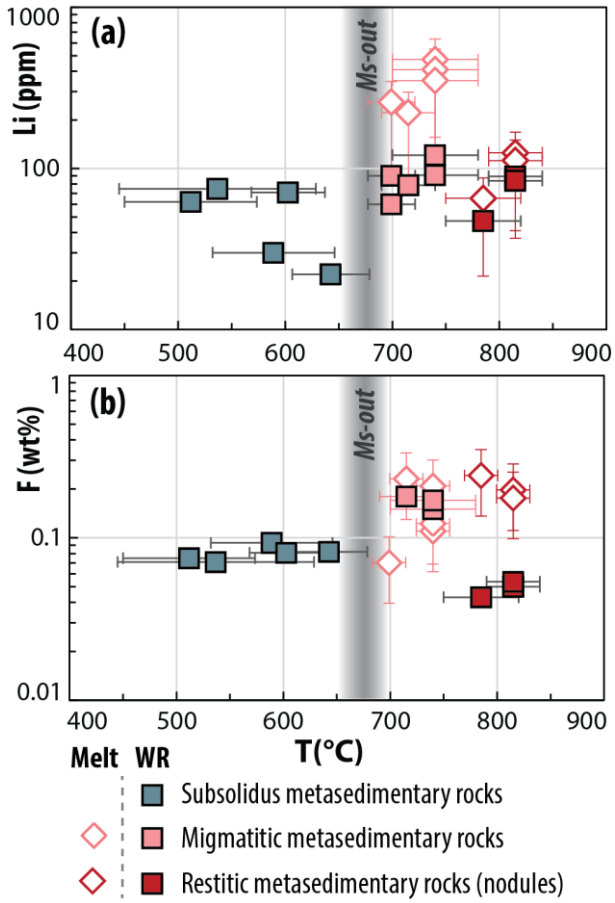

Fig. 12 Evolution of the whole-rock (WR) Li **a** and F **b** concentrations of metasedimentary rocks from the Velay dome as a function of peak temperature, and comparison with calculated melt compositions in equilibrium with biotite (using Kd values from Table 3).

Factors of Li-F enrichment in granitic melts during anatexis

Silicate mineral records and modeling results indicate that metapelite-derived melts systematically show modest Li contents, globally in the range of the concentration of the melt in equilibrium with biotite from the cordierite-bearing Velay granite (i.e., 130-540 ppm Li considering maximum and minimum $Kd^{Bt/melt}$ values, Figs. 8 to 11). Notwithstanding, "fluid-absent" melting favors the Li enrichment of anatectic melts relatively to "fluid-assisted" melting. An enrichment factor around 2 is observed for Li by changing the water concentration of the metapelite protolith from 3.0 to 1.8 wt% (Fig. 10a). This is because decreasing the water

contents reduces the dilution effect by changing the range of melt proportions from ~20-60 wt% to ~10-35 wt%. Similarly, the crystallization of peritectic cordierite during LP crustal melting limits the Li enrichment of silicate melts by a factor of 2 (Fig. 8).

Metapelite-derived melts relatively enriched in F (~ 0.15 wt% F) are produced at temperatures > 750°C near the biotite-out isograd (Figs. 9b and 11b). Such melts could be even more enriched (~0.4 wt%) if low temperature melts < 725°C are extracted from the melting zone (i.e., restite melting, Fig. 9d). However, the melts produced during restite melting are relatively Li poor ≤ 200 ppm (Fig. 9c), because Li, which is less compatible in biotite than F (Table 3), was removed/scavenged by lower temperature melts. Restite melting is, thus, not a viable process to generate Li-rich melts. Similarly, dehydration of restitic biotite-bearing deep crustal rocks in the presence of mantle-derived CO_2-rich fluids at granulite-facies conditions (Cuney and Barbey 2014) may generate a F-rich fluid but this media might not be especially enriched in Li due its major loss upon prograde melting at relatively low temperatures. Therefore, it is still unclear whether such metamorphic fluids could trigger the formation of Li-F-rich magmas during fluid-fluxed crustal melting in late-orogenic settings.

Modeling results indicate that fluid-absent melting of a peraluminous leucocratic orthogneiss can generate a melt that is concomitantly enriched in both F (~1 wt%) and Li (~600 ppm) at relatively low temperature (< 750°C, Figs. 9e,f and 10b). This is possible because (i) the small amounts of melt produced (~10-15 wt%) limit metal dilution, and (ii) the complete breakdown of both muscovite and biotite occurs within a narrow range of temperature (710-730˚C, Fig. 9e,f). This is consistent with our natural dataset as the melt in equilibrium with biotite from a Velay anatectic augen gneiss with peak temperature of 660-730°C (Couzinié et al. 2021) is characterized by concentrations of Li (~1,350 ppm) and F (~0.35 wt%), which are significantly higher than those of melts equilibrated with biotite from anatectic paragneisses (Fig. 6). The Li-F concentrations of orthogneiss-derived melts remain below that of the melt in

equilibrium with trioctahedral micas from the Fabras Li-mica-topaz granite (4,490-18,290 ppm Li; 1.0-2.5 wt% F) but are similar to that of the melt equilibrated with biotite from the muscovite-bearing granite (450-1,810 ppm Li; 0.6-1.5 wt% F).

Implications for the formation of peraluminous rare-metal granites and pegmatites

Our natural dataset and the results of geochemical modelling show that F-Li decoupling is expected during metapelite melting: the Li-richest melts would be produced at low temperature (< 750˚C) whereas the F-richest melts are more likely to be generated at > 750°C (Figs. 6, 9, 11, and Online Resource 3, Fig. S11). Such decoupling might affect other elements typically enriched up to economic levels in RMGPs. As for Li, the concentrations of W, Be and Cs in biotite from suprasolidus metasedimentary rocks decrease with increasing temperature (Online Resource 3, Fig. S7). Therefore, the melt rare-metal contents decreased as prograde melting proceeded, resulting in the production of the melts with the highest contents of W, Be and Cs at temperatures < 750˚C, by muscovite breakdown or incipient biotite breakdown. In contrast, Sn, Nb and Ta behaved like F as their concentrations in biotite remained constant or increased as melting reactions proceeded, suggesting that the richest melts were produced at temperatures > 750˚C.

Consistently, partial melting experiments performed on a biotite-rich paragneiss indicate that Li, Cs and W are enriched in the melt relatively to the protolith upon biotite-dehydration melting whereas the opposite is true for Nb and Ta (Michaud et al. 2021). Moreover, Zhao et al. (2022) predicted using a modeling approach that W-rich melts are generated at lower temperature (< 700°C) than Sn-rich ones (> 800°C) during metapelite melting. Mobilization of Sn only at high temperature (corresponding to biotite breakdown conditions), was also predicted by Wolf et al. (2018) based on the analyses of leucosomes and associated residuum of Variscan migmatites from Iberia. Therefore, Li-W-Be-Cs and F-Sn-Nb-Ta decoupling during partial melting of metapelites indicates that the latter are not adequate

sources for the generation of RMGPs which are characteristically enriched in *all* those elements. Low- and high temperature melts could be aggregated and mixed together in a same magmatic reservoir. In this case, however, dilution will occur, and the resulting hybrid melt will be depleted in rare-metals and F. Finally, a recent study showed that staurolite melting reactions can generate Li-rich melts (200-1,000 ppm) from a metapelitic protolith at MP conditions of 6-8 kbar (Knoll et al. 2023). Nonetheless, although staurolite may have high Li contents, it does not incorporate significant amount of other rare-metals (Nb, Ta, Sn, Cs) or F (Dutrow et al. 1986; Konzett et al. 2018; Knoll et al. 2023). Therefore, staurolite breakdown reactions (which are only relevant in metapelite systems) are likely not able to generate typical RMGPs as those encountered in the FMC.

In contrast, fluid-absent mica breakdown of a relatively biotite-poor and muscovite-rich peraluminous orthogneiss from 710 to 730°C generates a melt that is simultaneously enriched in both Li and F (Fig. 9e,f). Such melts would also be enriched in other metals incorporated in micas, such as Cs, Be, W, Nb, Ta and Sn. This is suggested by partial melting experiments performed on a muscovite-rich orthogneiss (Michaud et al. 2021) and our natural data indicating that orthogneiss biotite (and muscovite) has elevated Sn, Cs, W, Nb and Ta contents (Online Resources 2 and 3, Fig. S7). However, modeling the uptake of W, Sn, Ta and Nb by the melt phase remains elusive as these elements are also hosted in Fe-Ti oxide minerals (e.g., ilmenite, rutile) for which mineral/granitic melt partitioning data are scarce.

Despite the low melt fraction (~10 wt%, Fig. 9) produced by partial melting of orthogneisses, rare-metal-rich melts are expected to be readily extracted from their source. Indeed, considering melt H_2O and F contents of 8 and 1 wt%, respectively, yields a melt viscosity of ~10^4 Pa.s at 700°C (calculated using the model of Giordano et al. 2004). This value is low enough to ensure melt extraction from migmatitic sources during deformation (e.g., Vigneresse et al. 1996), and further rare-metal enrichment may occur by differentiation during

magma ascent and storage in magmatic reservoirs at upper crustal levels. Fractional crystallization modeling was performed to assess the capability of an orthogneiss-derived primary melt to reach the composition of the liquid equilibrated with the trioctahedral mica from the Fabras Li-mica-topaz granite (Li ~13,500 ppm, ~1.73 wt% F, Fig. 13). This is indeed possible moderating 80-90 wt% of fractional crystallization of an assemblage consisting of 5 wt% Ms, 5 wt% Bt and 90 wt% Qz-Fsp. In contrast, for the same degree of fractional crystallization, a metapelite-derived melt would only reach the composition of the melt in equilibrium with biotite from the muscovite-bearing granite (~1,350 ppm Li, ~1.03 wt% F, Fig. 13). Since the melt in equilibrium with trioctahedral mica from the Fabras granite features Li-F contents higher than or similar to those observed in economic grade RMGPs (e.g., the apical facies of the Beauvoir granite, with bulk Li and F of ~4,000–10,000 ppm and 1.5-2.5 wt%, respectively, Cuney et al. 1992; Raimbault et al. 1995), we conclude that orthogneiss melting followed by extended magmatic differentiation is a viable mechanism to form RMGP deposits.

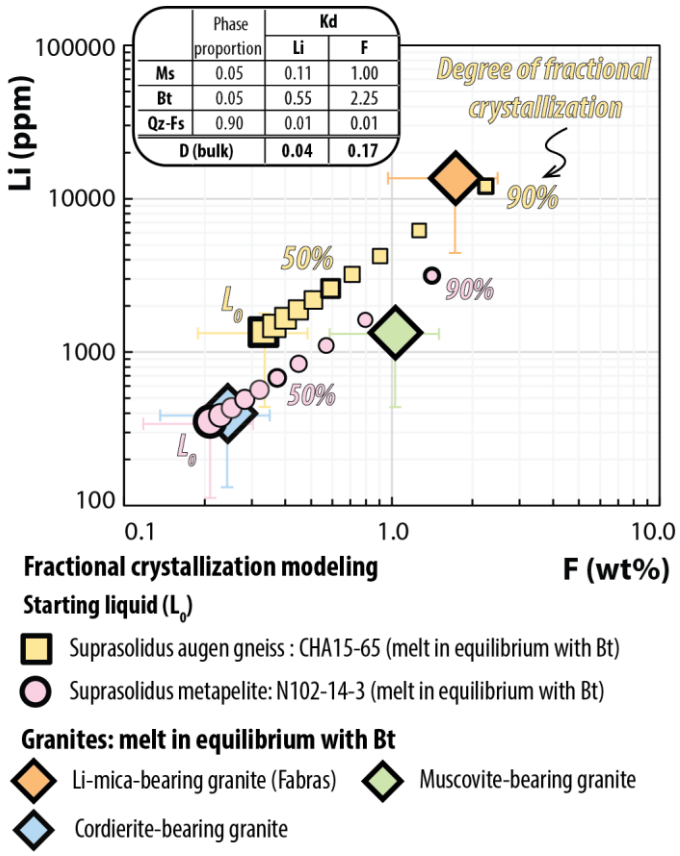

Fig. 13 Li vs. F concentration diagram illustrating the effect of fractional crystallization of micas and quartz-feldspar on the composition of primary melts (L_0) in equilibrium with trioctahedral micas from an anatectic metapelite and augen orthogneiss from the Velay dome. The degree of fractional crystallization is shown by increment of 10 wt% and the compositions of the melt in equilibrium with biotite from regional granites are reported for comparison. Error bars for granite melts and starting liquid compositions show deviations related to the use of minimum and maximum $Kd^{biotite/melt}$ values from the literature. Modeling parameters including phase proportions and Kd (preferred values of Table 3) are presented in inset.

The role of protracted crustal differentiation to generate Li-F-rich peraluminous rare-metal granites and pegmatites

Collectively, our results suggest a felsic meta-igneous source for Li-F-rich granites and possibly for RMGPs in general; their parental melts would derive from low temperature (< 750°C) melting of pre-existing peraluminous (meta-) granitic rocks followed by extended fractional crystallization. Such model would readily explain the abundance of RMGPs in the European Variscan belt since peraluminous orthogneisses constitute a major component of the pre-orogenic basement (Ballèvre et al. 2012; Chelle-Michou et al. 2017; García-Arias et al. 2018). They correspond to former S-type (volcano-) plutonic complexes that were formed during polycyclic crustal melting episodes extending from the Late Ediacaran to the Late Ordovician (550–445 Ma), i.e., 50–150 Ma before the onset of the Variscan orogeny. The oldest igneous rock suite (550–535 Ma) was emplaced in back-arc basins at the aftermath of the Cadomian accretionary orogeny (Linnemann et al. 2014; Mezger and Gerdes 2016; Couzinié et al. 2017). Additionally, many peraluminous granitic plutons and felsic volcanic rocks are remnants of a second, protracted (490–445 Ma) magmatic event (García-Arias et al. 2018) triggered by crustal extension coeval to the opening of the Rheic ocean (Nance et al. 2010).

A similar relationship between polycyclic crustal differentiation, involving repeated stages of granite melting followed by fractional crystallization, and the fertility of Archean terranes for Li-Cs-Ta pegmatites was highlighted by Černý (1989) and Kendall-Langley et al.

(2020). Therefore, we infer that the amenability of a given crustal segment to produce RMGPs during an orogenic cycle would necessarily be tied to its pre-orogenic evolution: terrains having experienced protracted crust differentiation with multiple episodes of crustal melting are expected be more rare-metal-fertile, as also proposed for U-rich leucogranites (Ballouard et al. 2018).

Conclusions

Geochemical analyses of silicate minerals from samples of the Velay anatectic dome, combined with geochemical modeling, allowed us to decipher the crustal melting conditions and protoliths amenable to generate Li-F-rich anatectic melts and RMGPs.

"Fluid-absent" melting favors the Li enrichment of anatectic melts relatively to "water-fluxed" melting because it produces lower melt amounts and thus limits the dilution of rare-metals. Low-pressure anatexis (< 5 kbar) leads to the crystallization of peritectic cordierite, which acts as a Li sink and hampers the Li transfer to silicate melts.

During metapelite anatexis, melts with the highest Li concentrations of 200-400 ppm are produced at temperature < 750°C upon muscovite breakdown or incipient biotite breakdown. The melt Li/F ratio decreases with increasing temperature and such decoupling precludes the formation of Li-F-rich melts with RMPG signatures. Restite melting at T > 750°C produces melts with the highest F contents (up to 0.4 wt%). However, prior loss of Li during the extraction of low temperature melts again impedes the generation of Li-F-rich silicic liquids.

"Fluid-absent" melting of a peraluminous orthogneiss at P > 5 kbar can produce melts simultaneously enriched in both F and Li due to near-concomitant muscovite and biotite breakdown within a narrow range of temperature (710-730°C) and the low amount of melt produced (~10 wt%), which limits dilution. An orthogneiss-derived melt with ~1,350 ppm Li and 0.3 wt% F (values estimated for a Velay anatectic orthogneiss based on biotite

compositions) can reach the Li-F enrichment of a peraluminous rare-metal granite (~10,000 ppm Li and 2 wt% F) after ~80-90 % of fractional crystallization. Given the composition of orthogneiss biotite and muscovite, the low-temperature orthogneiss-derived melts are also expected to be enriched in Cs, Be, W, Nb, Ta and Sn.

Therefore, the role of the protolith, especially the remelting of peraluminous granite along with further fractional crystallization, appears critical for the generation of Li-F-rich peraluminous granitic melts and RMGPs in general. This highlights the key role played by crustal recycling processes and tectonic-magmatic inheritance on the rare-metal fertility of a given crust segment.

Acknowledgments

This work, including the post-doctoral fellowship of C. Ballouard, was supported by the French National Research Agency through the national program 'Investissements d'avenir' with the reference ANR-10-LABX-21-RESSOURCES21 (including the project LabEx Li-Beauvoir supported by Imerys), the Grand Est region via the program 'Jeunes chercheurs' 2020, the ANR TRANSFAIR, as well as the CNRS/INSU program TelluS-2022. This study was initiated during the Master's internship of L. Gerard. This work beneficiated of stimulating discussions with L. France, N. Esteves and R. Romer. We are grateful to A. Flammang, J. Moine, A. Lecomte, L. Salsi, O. Rouer, C. Peiffert and E. Moreira for thin section preparations, µXRF imaging, and technical assistance during SEM, EPMA and LA-ICP-MS analyses. This manuscript benefited from the comments and advice of two anonymous reviewers, and from the guidance and editorial handling of O. Müntener.

References

Acosta-Vigil A, Buick I, Hermann J, Cesare B, Rubatto D, London D, Morgan GB (2010) Mechanisms of crustal anatexis: a geochemical study of partially melted metapelitic

enclaves and host dacite, SE Spain. J Petrol 51:785–821. https://doi.org/https://doi.org/10.1093/petrology/egp095

Alasino PH, Dahlquist JA, Galindo C, Casquet C, Saavedra J (2010) Andalusite and Na- and Li-rich cordierite in the La Costa pluton, Sierras Pampeanas, Argentina: Textural and chemical evidence for a magmatic origin. Int J Earth Sci 99:1051–1065. https://doi.org/10.1007/s00531-009-0445-1

Arnaud F, Boullier AM, Burg JP (2004) Shear structures and microstructures in micaschists: The Variscan Cévennes duplex (French Massif Central). J Struct Geol 26:855–868. https://doi.org/10.1016/j.jsg.2003.11.022

Ballèvre M, Fourcade S, Capdevila R, Peucat J-J, Cocherie A, Fanning CM (2012) Geochronology and geochemistry of Ordovician felsic volcanism in the Southern Armorican Massif (Variscan belt, France): Implications for the breakup of Gondwana. Gondwana Res 21:1019–1036. https://doi.org/10.1016/j.gr.2011.07.030

Ballouard C, Elburg MA, Tappe S, Reinke C, Ueckermann H, Doggart S (2020) Magmatic-hydrothermal evolution of rare metal pegmatites from the Mesoproterozoic Orange River pegmatite belt (Namaqualand, South Africa). Ore Geol Rev 116:103252. https://doi.org/10.1016/j.oregeorev.2019.103252

Ballouard C, Poujol M, Zeh A (2018) Multiple crust reworking in the French Armorican Variscan belt: implication for the genesis of uranium-fertile leucogranites. Int J Earth Sci 107:2317–2336. https://doi.org/10.1007/s00531-018-1600-3

Bambier A, Berger E-T, Mergoil J, Valadas B, Veyret Y, Weisbrod A (1985) Notice expicative de la feuille Burzet à 1/50 000, BRGM

Barbarin B (1999) A review of the relationships between granitoid types, their origins and their

geodynamic environments. Lithos 46:605–626. https://doi.org/10.1016/S0024-4937(98)00085-1

Barbey P, Marignac C, Montel JM, Macaudiere J, Gasquet D, Jabbori J (1999) Cordierite growth textures and the conditions of genesis and emplacement of crustal granitic magmas: the Velay granite complex (Massif Central, France). J Petrol 40:1425–1441. https://doi.org/https://doi.org/10.1093/petroj/40.9.1425

Barbey P, Villaros A, Marignac C, Montel JM (2015) Multiphase melting, magma emplacement and P-T-time path in late-collisional context: The Velay example (Massif Central, France). Bull la Soc Geol Fr 186:93–116. https://doi.org/10.2113/gssgfbull.186.2-3.93

Bea F, Montero P (1999) Behavior of accessory phases and redistribution of Zr, REE, Y, Th, and U during metamorphism and partial melting of metapelites in the lower crust: An example from the Kinzigite Formation of Ivrea-Verbano, NW Italy. Geochim Cosmochim Acta 63:1133–1153. https://doi.org/10.1016/S0016-7037(98)00292-0

Bea F, Pereira MD, Stroh A (1994) Mineral/leucosome trace-element partitioning in a peraluminous migmatite (a laser ablation-ICP-MS study). Chem Geol 117:291–312. https://doi.org/https://doi.org/10.1016/0009-2541(94)90133-3

Bertoldi C, Proyer A, Garbe-Schönberg D, Behrens H, Dachs E (2004) Comprehensive chemical analyses of natural cordierites: implications for exchange mechanisms. Lithos 78:389–409. https://doi.org/https://doi.org/10.1016/j.lithos.2004.07.003

Bhattacharya S (1993) Refinement of geothermobarometry for cordierite granulites. Proc Indian Acad Sci Planet Sci 102:537–545

Bouilhol P, Leyreloup AF, Delor C, Vauchez A, Monié P (2006) Relationships between lower and upper crust tectonic during doming: the mylonitic southern edge of the Velay

metamorphic core complex (Cévennes-French Massif Central). Geodin Acta 19:137–153. https://doi.org/https://doi.org/10.3166/ga.19.137-153

Černý P (1989) Contrasting geochemistry of two pegmatite fields in Manitoba: Products of juvenile Aphebian crust and polycyclic Archean evolution. Precambrian Res 45:215–234. https://doi.org/https://doi.org/10.1016/0301-9268(89)90041-7

Černý P, Chapman R, Schreyer W, Ottolini L, Bottazzi P, McCammon CA (1997) Lithium in sekaninaite from the type locality, Dolni Bory, Czech Republic. Can Mineral 35:167–173

Černý P, Ercit TS (2005) The classification of granitic pegmatites revisited. Can Mineral 43:2005–2026. https://doi.org/10.2113/gscanmin.43.6.2005

Černý P, Masau M, Goad BE, Ferreira K (2005) The Greer Lake leucogranite, Manitoba, and the origin of lepidolite-subtype granitic pegmatites. Lithos 80:305–321. https://doi.org/10.1016/j.lithos.2003.11.003

Chelle-Michou C, Laurent O, Moyen JF, Block S, Paquette JL, Couzinié S, Gardien V, Vanderhaeghe O, Villaros A, Zeh A (2017) Pre-Cadomian to late-Variscan odyssey of the eastern Massif Central, France: Formation of the West European crust in a nutshell. Gondwana Res 46:170–190. https://doi.org/10.1016/j.gr.2017.02.010

Connolly JAD (2009) The geodynamic equation of state: What and how. Geochemistry, Geophys Geosystems 10:. https://doi.org/10.1029/2009GC002540

Couzinié S, Bouilhol P, Laurent O, Grocolas T, Montel JM (2022) Cambro-Ordovician ferrosilicic magmatism along the northern Gondwana margin: constraints from the Cézarenque-Joyeuse gneiss complex (French Massif Central). BSGF - Earth Sci Bull 193:15. https://doi.org/10.1051/bsgf/2022010

Couzinié S, Bouilhol P, Laurent O, Marko L, Moyen JF (2021) When zircon drowns: Elusive

geochronological record of water-fluxed orthogneiss melting in the Velay dome (Massif Central, France). Lithos 384–385:105938. https://doi.org/10.1016/j.lithos.2020.105938

Couzinié S, Laurent O, Chelle-Michou C, Bouilhol P, Paquette JL, Gannoun AM, Moyen JF (2019) Detrital zircon U–Pb–Hf systematics of Ediacaran metasediments from the French Massif Central: Consequences for the crustal evolution of the north Gondwana margin. Precambrian Res 324:269–284. https://doi.org/10.1016/j.precamres.2019.01.016

Couzinié S, Laurent O, Poujol M, Mintrone M, Chelle-Michou C, Moyen JF, Bouilhol P, Vezinet A, Marko L (2017) Cadomian S-type granites as basement rocks of the Variscan belt (Massif Central, France): Implications for the crustal evolution of the north Gondwana margin. Lithos 286–287:16–34. https://doi.org/10.1016/j.lithos.2017.06.001

Cuney M, Alexandrov P, de Veslud CLC, Cheilletz A, Raimbault L, Ruffet G, Scaillet S (2002) The timing of W-Sn-rare metals mineral deposit formation in the Western Variscan chain in their orogenic setting: the case of the Limousin area (Massif Central, France). Geol Soc London, Spec Publ 204:213–228. https://doi.org/https://doi.org/10.1144/GSL.SP.2002.204.01.1

Cuney M, Barbey P (2014) Uranium, rare metals, and granulite-facies metamorphism. Geosci Front 5:729–745. https://doi.org/10.1016/j.gsf.2014.03.011

Cuney M, Marignac C, Weisbrod A (1992) The Beauvoir topaz-lepidolite albite granite (Massif Central, France); the disseminated magmatic Sn-Li-Ta-Nb-Be mineralization. Econ Geol 87:1766–1794. https://doi.org/https://doi.org/10.2113/gsecongeo.87.7.1766

Debon F, Le Fort P (1988) A cationic classification of common plutonic rocks and their magmatic associations: principles, method, applications. Bull Minéralogie 111:493–510

Dutrow BL, Holdaway MJ, Hinton RW (1986) Lithium in staurolite and its petrologic

significance. Contrib to Mineral Petrol 94:496–506. https://doi.org/10.1007/BF00376341

Evensen JM, London D (2003) Experimental partitioning of Be, Cs, and other trace elements between cordierite and felsic melt, and the chemical signature of S-type granite. Contrib to Mineral Petrol 144:739–757. https://doi.org/10.1007/s00410-002-0426-x

Faure M, Lardeaux JM, Ledru P (2009) A review of the pre-Permian geology of the Variscan French Massif Central. Comptes Rendus - Geosci 341:202–213. https://doi.org/10.1016/j.crte.2008.12.001

Finch EG, Tomkins AG (2017) Fluorine and chlorine behaviour during progressive dehydration melting: Consequences for granite geochemistry and metallogeny. J Metamorph Geol 35:739–757. https://doi.org/https://doi.org/10.1111/jmg.12253

Franz G, Morteani G (2002) Be-minerals: synthesis, stability, and occurrence in metamorphic rocks. Rev Mineral geochemistry 50:551–589. https://doi.org/https://doi.org/10.2138/rmg.2002.50.13

Fuhrman ML, Lindsley DH (1988) Ternary-feldspar modeling and thermometry. Am Mineral 73:201–215

García-Arias M, Díez-Montes A, Villaseca C, Blanco-Quintero IF (2018) The Cambro-Ordovician Ollo de Sapo magmatism in the Iberian Massif and its Variscan evolution: A review. Earth-Science Rev 176:345–372. https://doi.org/10.1016/j.earscirev.2017.11.004

Giordano D, Romano C, Dingwell DB, Poe B, Behrens H (2004) The combined effects of water and fluorine on the viscosity of silicic magmas. Geochim Cosmochim Acta 68:5159–5168. https://doi.org/https://doi.org/10.1016/j.gca.2004.08.012

Gordillo CE, Schreyer W, Werding G, Abraham K (1985) Lithium in NaBe-cordierites from El Peñón, Sierra de Córdoba, Argentina. Contrib to Mineral Petrol 90:93–100.

https://doi.org/10.1007/BF00373045

Gourcerol B, Gloaguen E, Melleton J, Tuduri J, Galiegue X (2019) Re-assessing the European lithium resource potential – A review of hard-rock resources and metallogeny. Ore Geol Rev 109:494–519. https://doi.org/10.1016/j.oregeorev.2019.04.015

Hanson GN (1978) The application of trace elements to the petrogenesis of igneous rocks of granitic composition. Earth Planet Sci Lett 38:26–43. https://doi.org/10.1016/0012-821X(78)90124-3

Harlaux M (2016) Tungsten and rare-metal (Nb, Ta, Sn) hydrothermal metallogenic systems in the late-variscan orogenic context : example of the French Massif Central. Dissertation, Université de Lorraine

Harlaux M, Mercadier J, Bonzi WM-E, Kremer V, Marignac C, Cuney M (2017) Geochemical signature of magmatic-hydrothermal fluids exsolved from the Beauvoir Rare-Metal Granite (Massif Central, France): insights from LA-ICPMS analysis of primary fluid inclusions. Geofluids 2017:1925817. https://doi.org/https://doi.org/10.1155/2017/1925817

Henry DJ, Guidotti C V., Thomson JA (2005) The Ti-saturation surface for low-to-medium pressure metapelitic biotites: Implications for geothermometry and Ti-substitution mechanisms. Am Mineral 90:316–328. https://doi.org/10.2138/am.2005.1498

Herron MM (1988) Geochemical classification of terrigenous sands and shales from core or log data. J Sediment Res 58:820–829. https://doi.org/https://doi.org/10.1306/212F8E77-2B24-11D7-8648000102C1865D

Holdaway MJ (2001) Recalibration of the GASP geobarometer in light of recent garnet and plagioclase activity models and versions of the garnet-biotite geothermometer. Am

Mineral 86:1117–1129. https://doi.org/https://doi.org/10.2138/am-2001-1001

Holdaway MJ (2000) Application of new experimental and garnet Margules data to the garnet-biotite geothermometer. Am Mineral 85:881–892. https://doi.org/https://doi.org/10.2138/am-2000-0701

Hulsbosch N, Hertogen J, Dewaele S, André L, Muchez P (2014) Alkali metal and rare earth element evolution of rock-forming minerals from the Gatumba area pegmatites (Rwanda): Quantitative assessment of crystal-melt fractionation in the regional zonation of pegmatite groups. Geochim Cosmochim Acta 132:349–374. https://doi.org/10.1016/j.gca.2014.02.006

Icenhower J, London D (1995) An experimental study of element partitioning among biotite, muscovite, and coexisting peraluminous silicic melt at 200 MPa (H_2O). Am Mineral 80:1229–1251. https://doi.org/10.2138/am-1995-11-1213

Janoušek V, Moyen J-F (2020) Whole-rock geochemical modelling of granite genesis: the current state of play. Geol Soc London, Spec Publ 491:267–291. https://doi.org/https://doi.org/10.1144/SP491-2018-160

Kaeter D, Barros R, Menuge JF, Chew DM (2018) The magmatic–hydrothermal transition in rare-element pegmatites from southeast Ireland: LA-ICP-MS chemical mapping of muscovite and columbite–tantalite. Geochim Cosmochim Acta 240:98–130. https://doi.org/10.1016/j.gca.2018.08.024

Kendall-Langley LA, Kemp AIS, Grigson JL, Hammerli J (2020) U-Pb and reconnaissance Lu-Hf isotope analysis of cassiterite and columbite group minerals from Archean Li-Cs-Ta type pegmatites of Western Australia. Lithos 352–353:105231. https://doi.org/10.1016/j.lithos.2019.105231

Knoll T, Huet B, Schuster R, Mali H, Ntaflos T, Hauzenberger C (2023) Lithium pegmatite of anatectic origin-A case study from the Austroalpine Unit Pegmatite Province (Eastern European Alps): geological data and geochemical model. Ore Geol Rev 154:105298. https://doi.org/https://doi.org/10.1016/j.oregeorev.2023.105298

Knoll T, Schuster R, Huet B, Mali H, Onuk P, Horschinegg M, Ertl A, Giester G (2018) Spodumene pegmatites and related leucogranites from the austroalpine unit (Eastern Alps, central europe): Field relations, petrography, geochemistry, and geochronology. Can Mineral 56:489–528. https://doi.org/10.3749/canmin.1700092

Konzett J, Hauzenberger C, Ludwig T, Stalder R (2018) Anatectic granitic pegmatites from the Eastern Alps: A case of variable rare metal enrichment during high-grade regional metamorphism. II: Pegmatite staurolite as an indicator of anatectic pegmatite parent melt formation - a field and experimental study. Can Mineral 56:603–624. https://doi.org/10.3749/canmin.1800011

Korhonen FJ, Brown M, Clark C, Bhattacharya S (2013) Osumilite–melt interactions in ultrahigh temperature granulites : phase equilibria modelling and implications for the P–T–t evolution of the Eastern Ghats Province, India. J Metamorph Geol 31:881–907. https://doi.org/10.1111/jmg.12049

Kunz BE, Warren CJ, Jenner FE, Harris NBW, Argles TW (2022) Critical metal enrichment in crustal melts: The role of metamorphic mica. Geology. https://doi.org/https://doi.org/10.1130/G50284.1

Laurent O, Couzinié S, Zeh A, Vanderhaeghe O, Moyen J-F, Villaros A, Gardien V, Chelle-Michou C (2017) Protracted, coeval crust and mantle melting during Variscan late-orogenic evolution: U–Pb dating in the eastern French Massif Central. Int J Earth Sci 421–451. https://doi.org/10.1007/s00531-016-1434-9

Ledru P, Courrioux G, Dallain C, Lardeaux JM, Montel JM, Vanderhaeghe O, Vitel G (2001) The Velay dome (French Massif Central): melt generation and granite emplacement during orogenic evolution. Tectonophysics 342:207–237. https://doi.org/10.1016/S0040-1951(01)00165-2

Linnemann U, Gerdes A, Hofmann M, Marko L (2014) The Cadomian Orogen : Neoproterozoic to Early Cambrian crustal growth and orogenic zoning along the periphery of the West African Craton — Constraints from U – Pb zircon ages and Hf isotopes. Precambrian Res 244:236–278. https://doi.org/10.1016/j.precamres.2013.08.007

Linnen RL, Cuney M (2005) Granite-related rare-element deposits and experimental constraints on Ta-Nb-W-Sn-Zr-Hf mineralization, in Linnen RL and Samson IM, eds., rare-element geochemistry and mineral deposits. In: Geological Association of Canada, GAC, Short Course

Linnen RL, Van Lichtervelde M, Černý P (2012) Granitic Pegmatites as Sources of Strategic Metals. Elements 8:275–280. https://doi.org/10.2113/gselements.8.4.275

London D (2018) Ore-forming processes within granitic pegmatites. Ore Geol Rev 101:349–383. https://doi.org/https://doi.org/10.1016/j.oregeorev.2018.04.020

Lotout C, Poujol M, Pitra P, Anczkiewicz R, Van Den Driessche J (2020) From burial to exhumation: emplacement and metamorphism of mafic eclogitic terranes constrained through multimethod petrochronology, case study from the Lévézou Massif (French Massif Central, Variscan Belt). J Petrol 61:egaa046. https://doi.org/https://doi.org/10.1093/petrology/egaa046

Marignac C, Cuney M (1999) Ore deposits of the French Massif Central: insight into the metallogenesis of the Variscan collision belt. Miner Depos 34:472–504. https://doi.org/10.1007/s001260050216

Mezger JE, Gerdes A (2016) Early Variscan (Visean) granites in the core of central Pyrenean gneiss domes: Implications from laser ablation U-Pb and Th-Pb studies. Gondwana Res 29:181–198. https://doi.org/10.1016/j.gr.2014.11.010

Michaud JA-S, Pichavant M, Villaros A (2021) Rare elements enrichment in crustal peraluminous magmas: insights from partial melting experiments. Contrib to Mineral Petrol 176:96. https://doi.org/10.1007/s00410-021-01855-9

Mohammadi A, Burg J-P, Bouilhol P, Ruh J (2016) U-Pb geochronology and geochemistry of Zahedan and Shah Kuh plutons, southeast Iran: Implication for closure of the South Sistan suture zone. Lithos 248:293–308. https://doi.org/https://doi.org/10.1016/j.lithos.2016.02.003

Monnier L, Salvi S, Melleton J, Lach P, Pochon A, Bailly L, Béziat D, De Parseval P (2022) Mica trace-element signatures: Highlighting superimposed W-Sn mineralizations and fluid sources. Chem Geol 600:120866. https://doi.org/10.1016/j.chemgeo.2022.120866

Montel J-M, Abdelghaffar R (1993) Les granites tardimigmatitiques du Velay (Massif central): principales caractéristiques pétrographiques et géochimiques. Géologie la Fr 15–28

Montel JM, Marignac C, Barbey P, Pichavant M (1992) Thermobarometry and granite genesis: the Hercynian low-P, high-T Velay anatectic dome (French Massif Central). J Metamorph Geol 10:1–15. https://doi.org/https://doi.org/10.1111/j.1525-1314.1992.tb00068.x

Moyen J-F, Laurent O, Chelle-Michou C, Couzinié S, Vanderhaeghe O, Zeh A, Villaros A, Gardien V (2017) Collision vs. subduction-related magmatism: Two contrasting ways of granite formation and implications for crustal growth. Lithos 277:154–177. https://doi.org/10.1016/j.lithos.2016.09.018

Müller A, Romer RL, Pedersen RB (2017) The Sveconorwegian pegmatite province - thousands

of pegmatites without parental granites. Can Mineral 55:283–315. https://doi.org/10.3749/canmin.1600075

Nance RD, Gutiérrez-Alonso G, Keppie JD, Linnemann U, Murphy JB, Quesada C, Strachan RA, Woodcock NH (2010) Evolution of the Rheic Ocean. Gondwana Res 17:194–222. https://doi.org/10.1016/j.gr.2009.08.001

Neves LJPF (1997) Trace element content and partitioning between biotite and muscovite of granitic rocks: a study in the Viseu region (Central Portugal). Eur J Mineral 9:849–858. https://doi.org/10.1127/ejm/9/4/0849

Patiño-Douce AE (1999) What do experiments tell us about the relative contributions of crust and mantle to the origin of granitic magmas? Geol Soc London, Spec Publ 168:55–75. https://doi.org/10.1144/GSL.SP.1999.168.01.05

Pfister JD, Kontak DJ, Groat LA (2023) Textural and mineralogical evolution of the Little Nahanni pegmatite group (NWT, Canada) with implications for metasomatism, rare-metal mineralization, and pegmatite-wall rock interaction. Can J Mineral Petrol 61:467–505. https://doi.org/10.3749/2000086

Pichavant M (2022) Experimental crystallization of the Beauvoir granite as a model for the evolution of Variscan rare metal magmas. J Petrol 63:egac120. https://doi.org/https://doi.org/10.1093/petrology/egac120

Pichavant M, Herrera JV, Boulmier S, Briqueu L, Joron J-L, Juteau M, Marin L, Michard A, Sheppard SMF, Treuil M, Vernet M (1987) The Macusani glasses, SE Peru: evidence of chemical fractionation in peraluminous magmas. Magmat Process Physicochem Princ Geochem Soc Spec Publ 1:359–373

Pichavant M, Kontak DJ, Briqueu L, Herrera JV, Clark AH (1988) The Miocene-Pliocene

Macusani Volcanics, SE Peru: I. Mineralogy and magmatic evolution of a two-mica aluminosilicate-bearing ignimbrite suite. Contrib to Mineral Petrol 100:300–324. https://doi.org/10.1007/BF00379742

Qiu L, Rudnick RL, McDonough WF, Bea F (2011) The behavior of lithium in amphibolite- to granulite-facies rocks of the Ivrea-Verbano Zone, NW Italy. Chem Geol 289:76–85. https://doi.org/10.1016/j.chemgeo.2011.07.014

Raimbault L, Burnol L (1998) The Richemont rhyolite dyke, Massif Central, France; a subvolcanic equivalent of rare-metal granites. Can Mineral 36:265–282

Raimbault L, Cuney M, Azencott C, Duthou J-L, Joron JL (1995) Geochemical evidence for a multistage magmatic genesis of Ta-Sn-Li mineralization in the granite at Beauvoir, French Massif Central. Econ Geol 90:548–576. https://doi.org/https://doi.org/10.2113/gsecongeo.90.3.548

Roda-Robles E, Villaseca C, Pesquera A, Gil-Crespo PP, Vieira R, Lima A, Garate-Olave I (2018) Petrogenetic relationships between Variscan granitoids and Li-(F-P)-rich aplite-pegmatites in the Central Iberian Zone: Geological and geochemical constraints and implications for other regions from the European Variscides. Ore Geol Rev 95:408–430. https://doi.org/10.1016/j.oregeorev.2018.02.027

Romer RL, Kroner U (2015) Sediment and weathering control on the distribution of Paleozoic magmatic tin–tungsten mineralization. Miner Depos 50:327–338. https://doi.org/10.1007/s00126-014-0540-5

Romer RL, Kroner U (2016) Phanerozoic tin and tungsten mineralization—Tectonic controls on the distribution of enriched protoliths and heat sources for crustal melting. Gondwana Res 31:60–95. https://doi.org/10.1016/j.gr.2015.11.002

Romer RL, Pichavant M (2021) Rare Metal Granites and Pegmatites. In: Alderton D, Elias SA (eds) Encyclopedia of Geology, 2nd edn. United Kingdom, Academic Press, pp 840-846. https://doi.org/10.1016/b978-0-08-102908-4.00003-5

Sallet R, Price JD, Ribeiro C, Hollanda MHBM, Sayeg IJ, Harlov D (2023) Fluorine behavior during experimental muscovite dehydration melting and natural partitioning between micas: Implications for the petrogenesis of peraluminous leucogranites and pegmatites. Am Mineral 108:1201–1212. https://doi.org/10.2138/am-2022-8663

Simons B, Andersen JCØ, Shail RK, Jenner FE (2017) Fractionation of Li, Be, Ga, Nb, Ta, In, Sn, Sb, W and Bi in the peraluminous Early Permian Variscan granites of the Cornubian Batholith: Precursor processes to magmatic-hydrothermal mineralisation. Lithos 278–281:491–512. https://doi.org/10.1016/j.lithos.2017.02.007

Simons B, Shail RK, Andersen JCØ (2016) The petrogenesis of the Early Permian Variscan granites of the Cornubian Batholith: Lower plate post-collisional peraluminous magmatism in the Rhenohercynian Zone of SW England. Lithos 260:76–94. https://doi.org/10.1016/j.lithos.2016.05.010

Stewart DB (1978) Petrogenesis of lithium-rich pegmatites. Am Mineral 63:970–980

Thierry J, Marignac C, Ledru P, Reboulet S, Dagain J, Naud G, Roger J, Laumonier B, Vernhet Y (2014) Notice explicative de la feuille de Privas à 1/5000, BRGM

Tischendorf G, Gottesmann B, Foerster H-J, Trumbull RB (1997) On Li-bearing micas: estimating Li from electron microprobe analyses and an improved diagram for graphical representation. Mineral Mag 61:809–834. https://doi.org/10.1180/minmag.1997.061.409.05

Toteu SF, Macaudiere J (1984) Complex synkinematic and postkinematic garnet porphyroblast

growth in polymetamorphic rocks. J Struct Geol 6:669–677. https://doi.org/https://doi.org/10.1016/0191-8141(84)90005-1

Tropper P, Wyhlidal S, Haefeker UA, Mirwald PW (2018) An experimental investigation of Na incorporation in cordierite in low P/high T metapelites. Mineral Petrol 112:199–217. https://doi.org/10.1007/s00710-017-0522-2

Turpin L, Cuney M, Friedrich M, Bouchez J-L, Aubertin M (1990) Meta-igneous origin of Hercynian peraluminous granites in N.W. French Massif Central: implications for crustal history reconstructions. Contrib to Mineral Petrol 104:163–172. https://doi.org/10.1007/BF00306440

Vanderhaeghe O, Laurent O, Gardien V, Moyen JF, Gébelin A, Chelle-Michou C, Couzinié S, Villaros A, Bellanger M (2020) Flow of partially molten crust controlling construction, growth and collapse of the Variscan orogenic belt: The geologic record of the French Massif Central. BSGF - Earth Sci Bull 191:25. https://doi.org/10.1051/bsgf/2020013

Vielzeuf D, Holloway JR (1988) Experimental determination of the fluid-absent melting relations in the pelitic system. Contrib to Mineral Petrol 98:257–276. https://doi.org/10.1007/BF00375178

Vigneresse JL, Barbey P, Cuney M (1996) Rheological Transitions During Partial Melting and Crystallization with Application to Felsic Magma Segregation and Transfer. J Petrol 37:1579–1600. https://doi.org/10.1093/petrology/37.6.1579

Villaros A, Laurent O, Couzinié S, Moyen JF, Mintrone M (2018) Plutons and domes: the consequences of anatectic magma extraction—example from the southeastern French Massif Central. Int J Earth Sci 107:2819–2842. https://doi.org/10.1007/s00531-018-1630-x

Villaros A, Pichavant M (2019) Mica-liquid trace elements partitioning and the granite-pegmatite connection: The St-Sylvestre complex (Western French Massif Central). Chem Geol 528:119265. https://doi.org/10.1016/j.chemgeo.2019.07.040

Weber C, Barbey P (1986) The role of water, mixing processes and metamorphic fabric in the genesis of the Baume Migmatites (Ardeche, France). Contrib to Mineral Petrol 92:481–491. https://doi.org/10.1007/BF00374430

Weinberg RF, Hasalová P (2015) Water-fluxed melting of the continental crust: A review. Lithos 212–215:158–188. https://doi.org/10.1016/j.lithos.2014.08.021

Weisbrod A (1968) Les conditions du métamorphisme dans les Cévennes médianes (Massif Central, France). CR Acad Sci Paris 266:755–757

White RW, Powell R, Holland TJB, Johnson TE, Green ECR (2014) New mineral activity-composition relations for thermodynamic calculations in metapelitic systems. J Metamorph Geol 32:261–286. https://doi.org/10.1111/jmg.12071

Whitney DL, Evans BW (2010) Abbreviations for names of rock-forming minerals. Am Mineral 95:185–187. https://doi.org/https://doi.org/10.2138/am.2010.3371

Williamson BJ, Downes H, Thirlwall MF, Beard A (1997) Geochemical constraints on restite composition and unmixing in the Velay anatectic granite, French Massif Central. Lithos 40:295–319. https://doi.org/https://doi.org/10.1016/S0024-4937(97)00033-9

Wolf M, Romer RL, Franz L, López-moro FJ (2018) Tin in granitic melts : The role of melting temperature and protolith composition. Lithos 310–311:20–30. https://doi.org/10.1016/j.lithos.2018.04.004

Wu CM, Chen HX (2015) Revised Ti-in-biotite geothermometer for ilmenite- or rutile-bearing crustal metapelites. Sci Bull 60:116–121. https://doi.org/10.1007/s11434-014-0674-y

Yardley BWD, Barber JP (1991) Melting reactions in the Connemara Schists: the role of water infiltration in the formation of amphibolite facies migmatites. Am Mineral 76:848–856

Zhao P, Chu X, Williams-Jones AE, Mao J, Yuan S (2022) The role of phyllosilicate partial melting in segregating tungsten and tin deposits in W-Sn metallogenic provinces. Geology 50:121–125. https://doi.org/10.1130/G49248.1

Zhou JS, Wang Q, Xu YG, Cempírek J, Wang H, Ma JL, Wei GJ, Huang TY, Zhu GH, Zhang L (2021) Geochronology, petrology, and lithium isotope geochemistry of the Bailongshan granite-pegmatite system, northern Tibet: Implications for the ore-forming potential of pegmatites. Chem Geol 584:120484. https://doi.org/10.1016/j.chemgeo.2021.120484

Figure 1

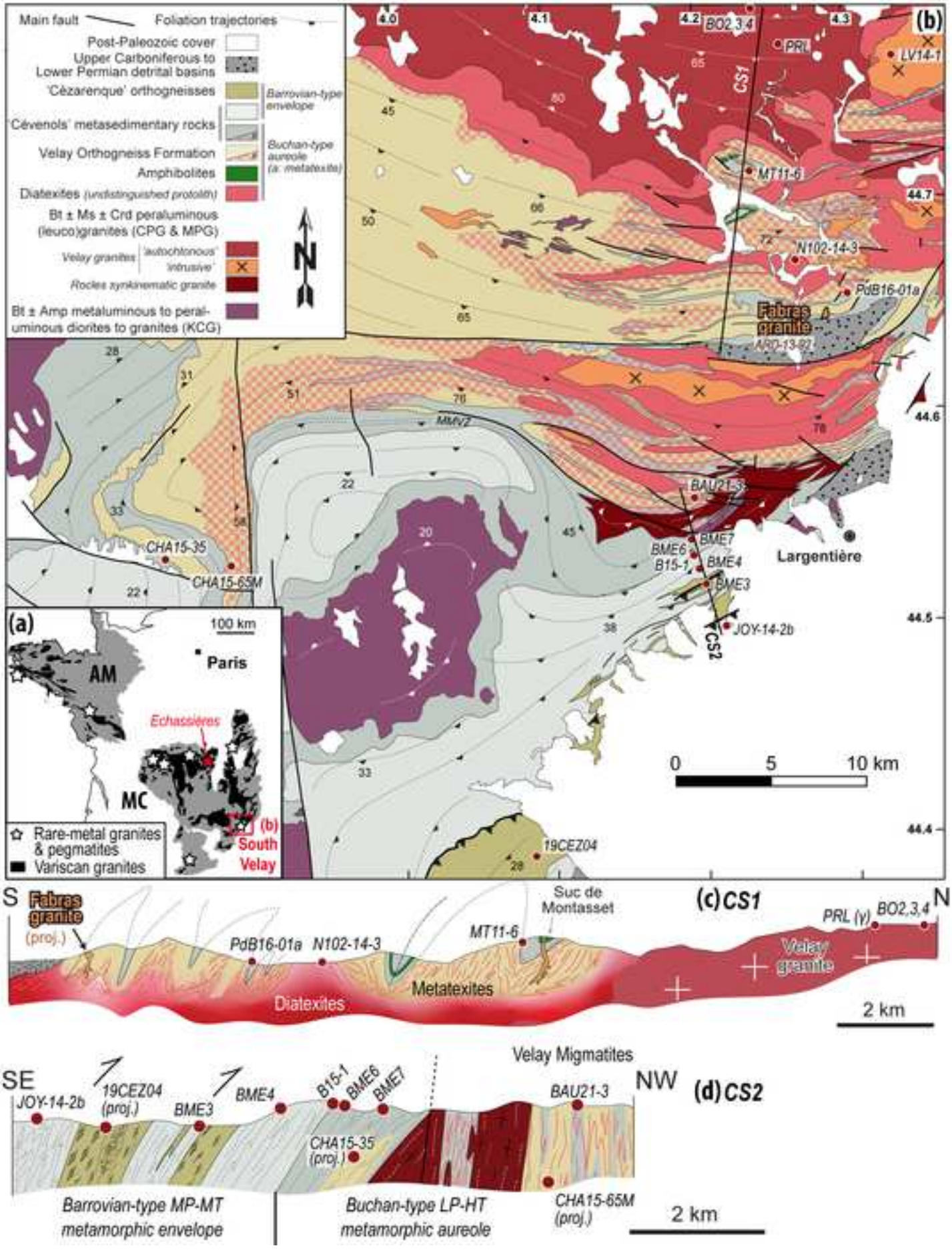

Figure 2

Click here to access/download;Figure;Fig.2-R1.tif

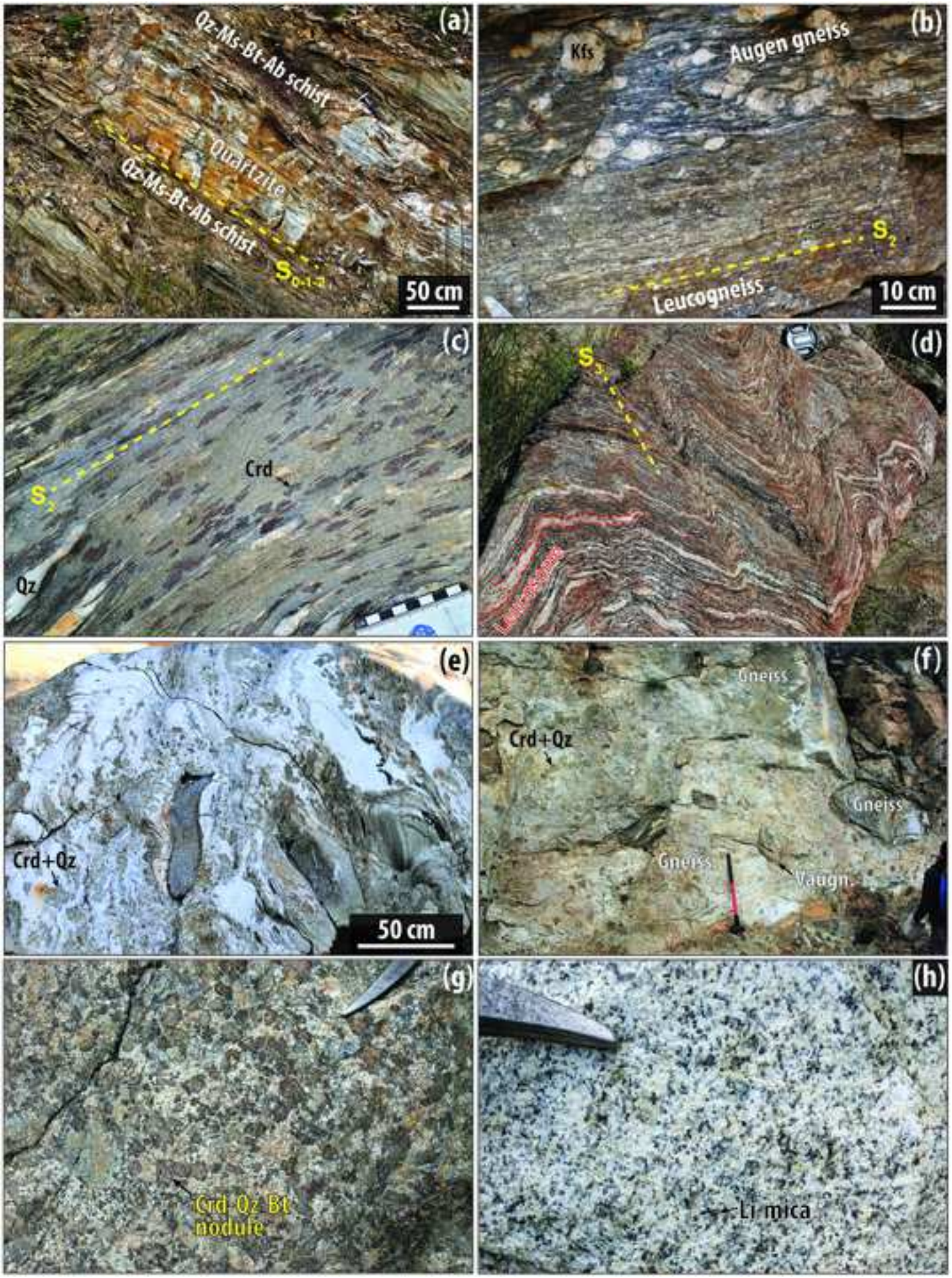

Figure 3

Click here to access/download;Figure;Fig.3-R1.tif

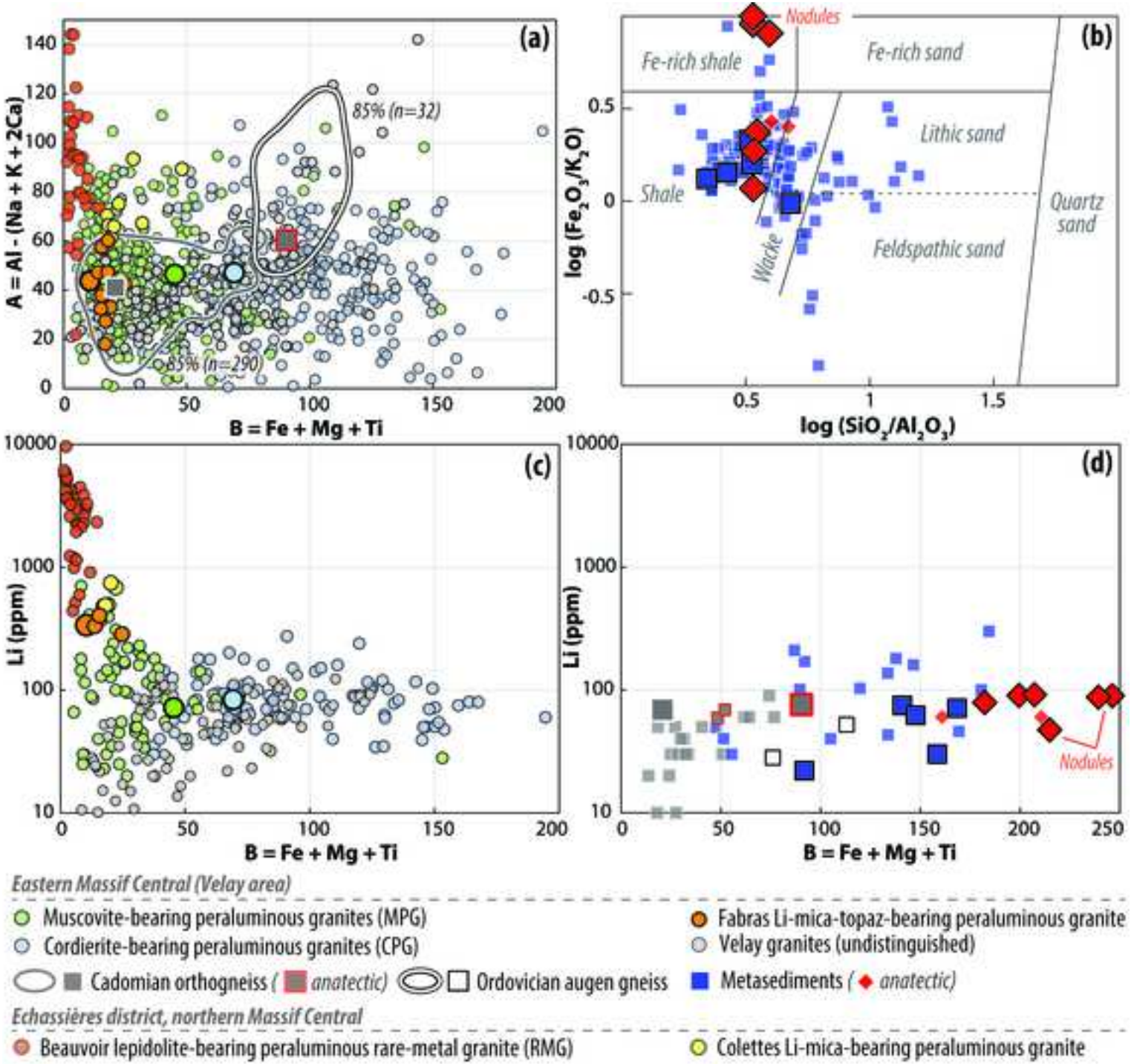

Figure 4

Click here to access/download;Figure;Fig.4-R1.tif

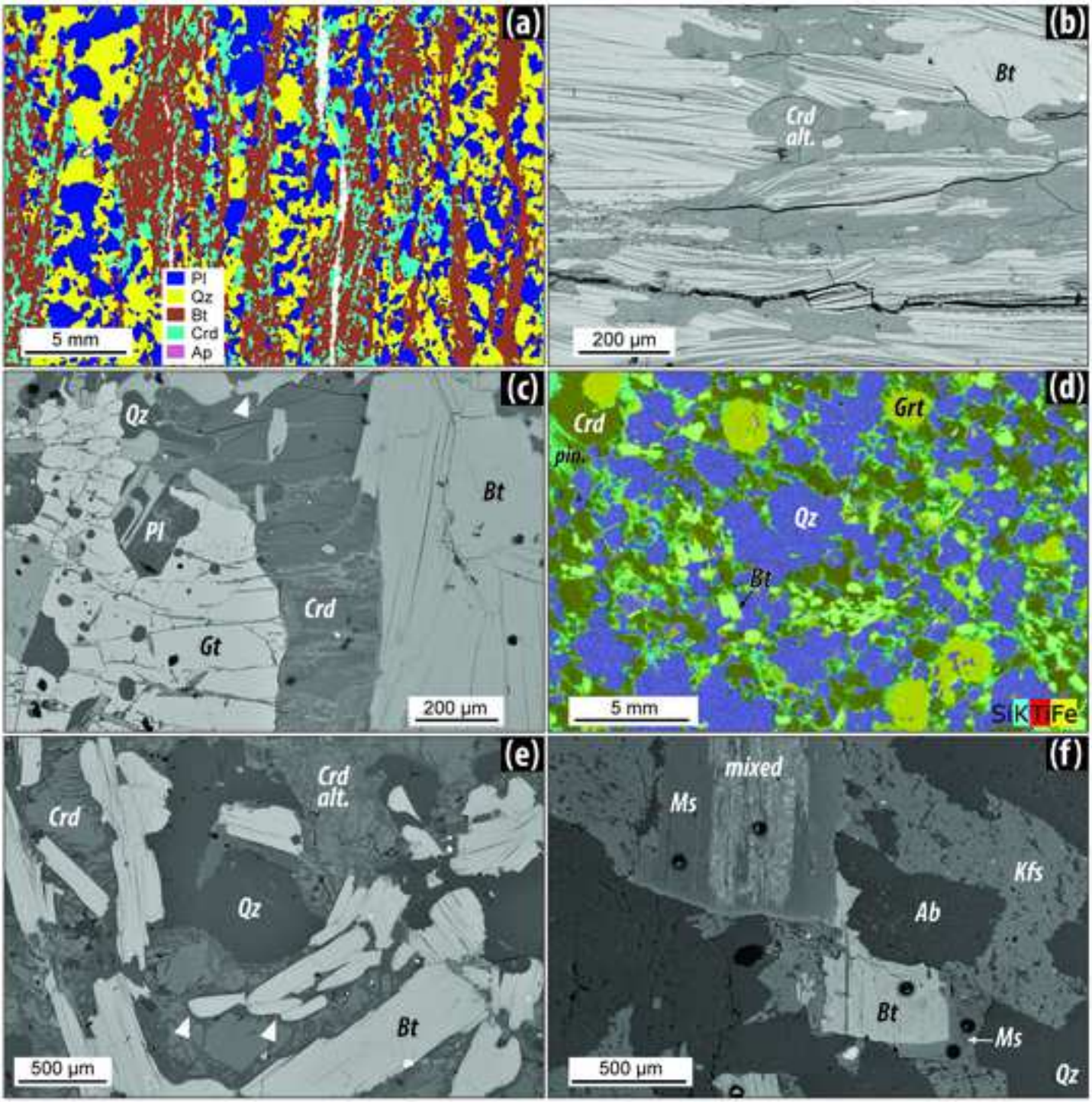

Figure 5

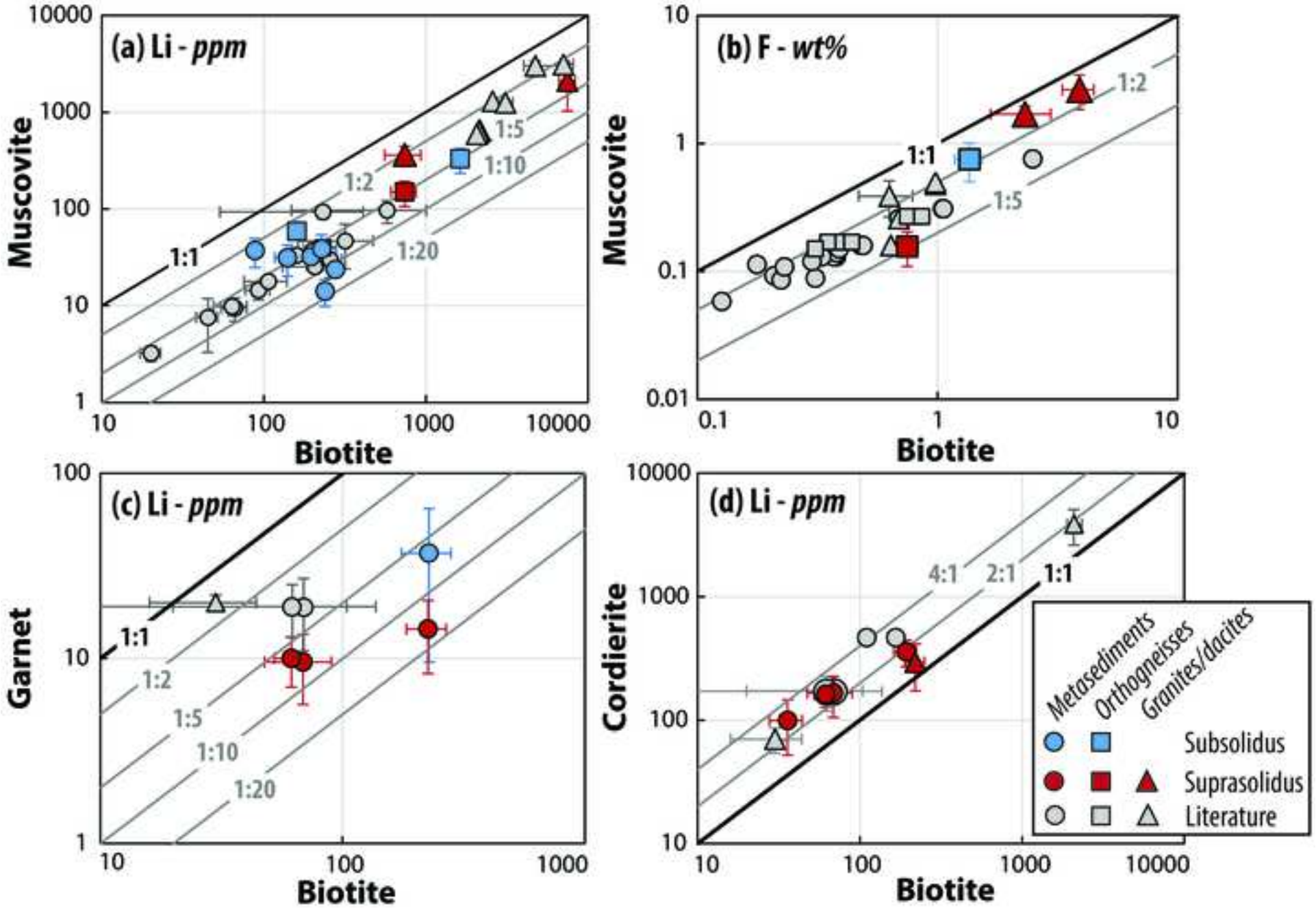

Figure 6

Click here to access/download;Figure;Fig.6-R1.tif

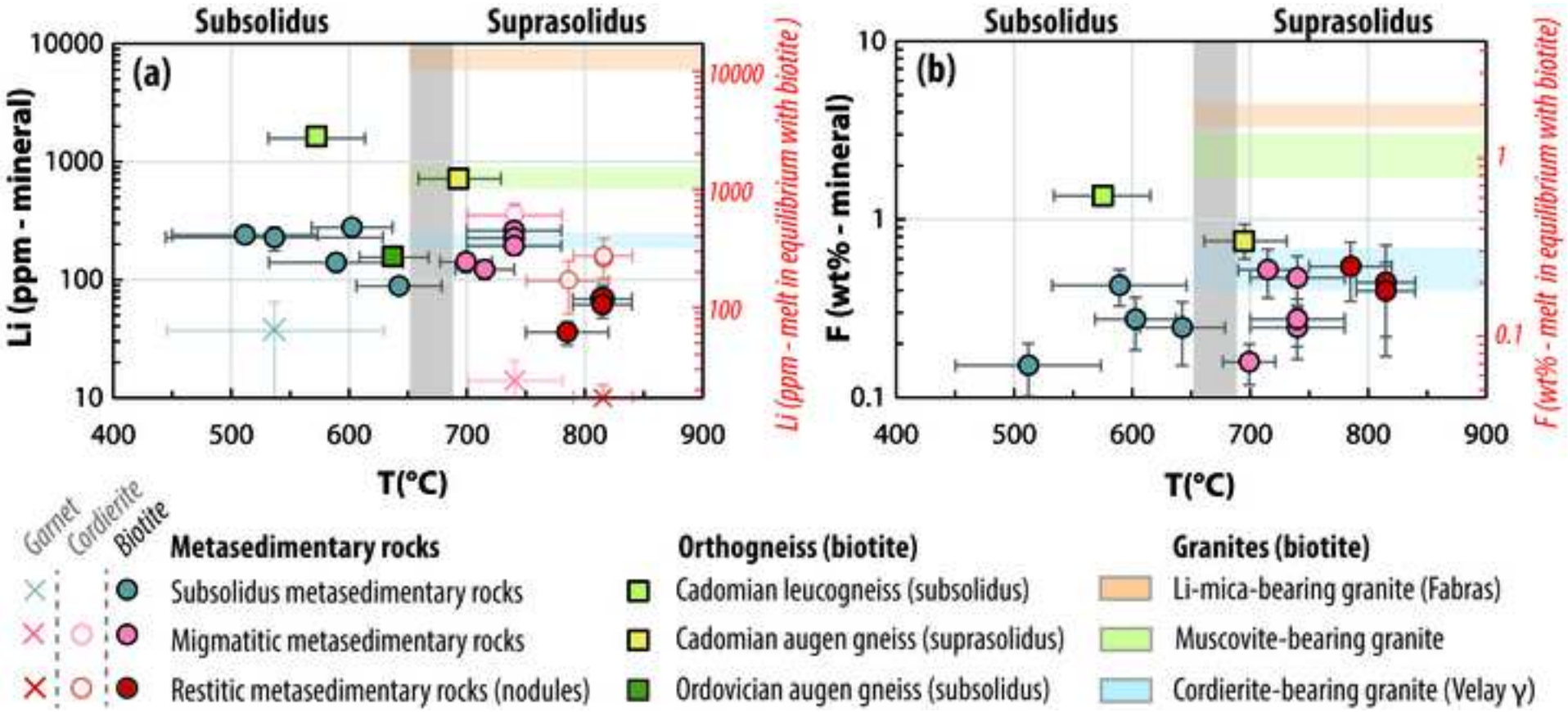

Figure 7

Click here to access/download;Figure;Fig.7-R1.tif

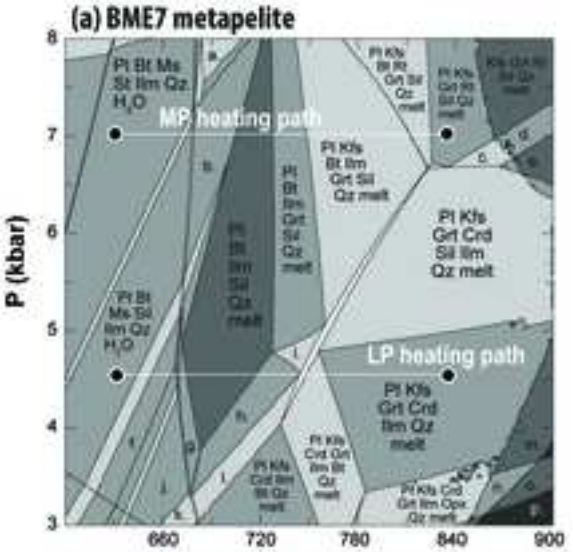

a. Pl Bt Ms Grt Ky Qz Ilm melt
b. Pl Bt Ms Sil Qz Ilm melt
c. Pl Kfs Grt Sil Qz Rt Ilm melt
d. Kfs Grt Sil Qz Rt Ilm melt
e. Kfs Grt Sil Qz Ilm melt
f. Pl Bt Ms Sil Qz Rt H_2O
g. Pl Bt Sil Qz Ilm melt H_2O
h. Pl Bt Crd Sil Qz Ilm melt
i. Pl Bt Grt Crd Sil Qz Ilm melt
j. Pl Kfs Bt Sil Qz Ilm H_2O
k. Pl Kfs Bt Crd Sil Qz Ilm H_2O
l. Pl Kfs Bt Crd Sil Qz Ilm melt
m. Kfs Grt Crd Qz Ilm melt
n. Kfs Grt Crd Opx Qz Ilm melt
o. Kfs Grt Crd Opx Ilm melt
p. Kfs Crd Opx Ilm melt

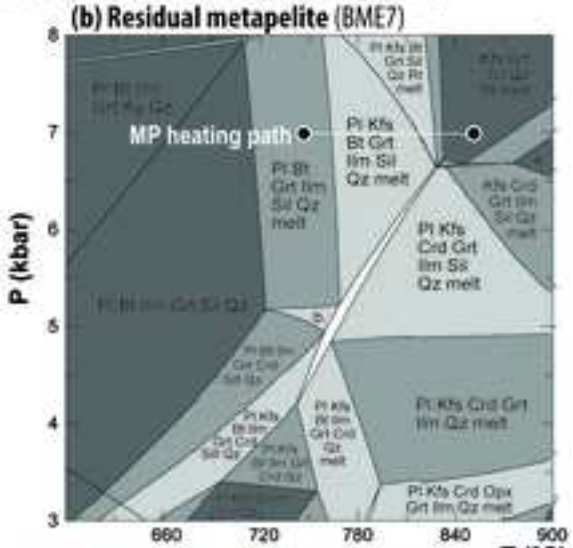

a. Kfs Grt Sil Qz Ilm melt
b. Pl Bt Ilm Crd Grt Sil Qz melt

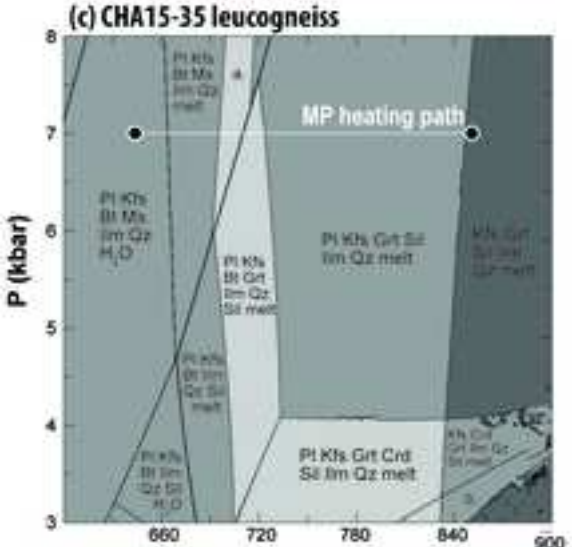

a. Pl Kfs Grt Bt Ms Ilm Qz melt
b. Kfs Crd Grt Ilm Qz Sp melt
c. Kfs Grt Ilm Qz Sp melt

Figure 8

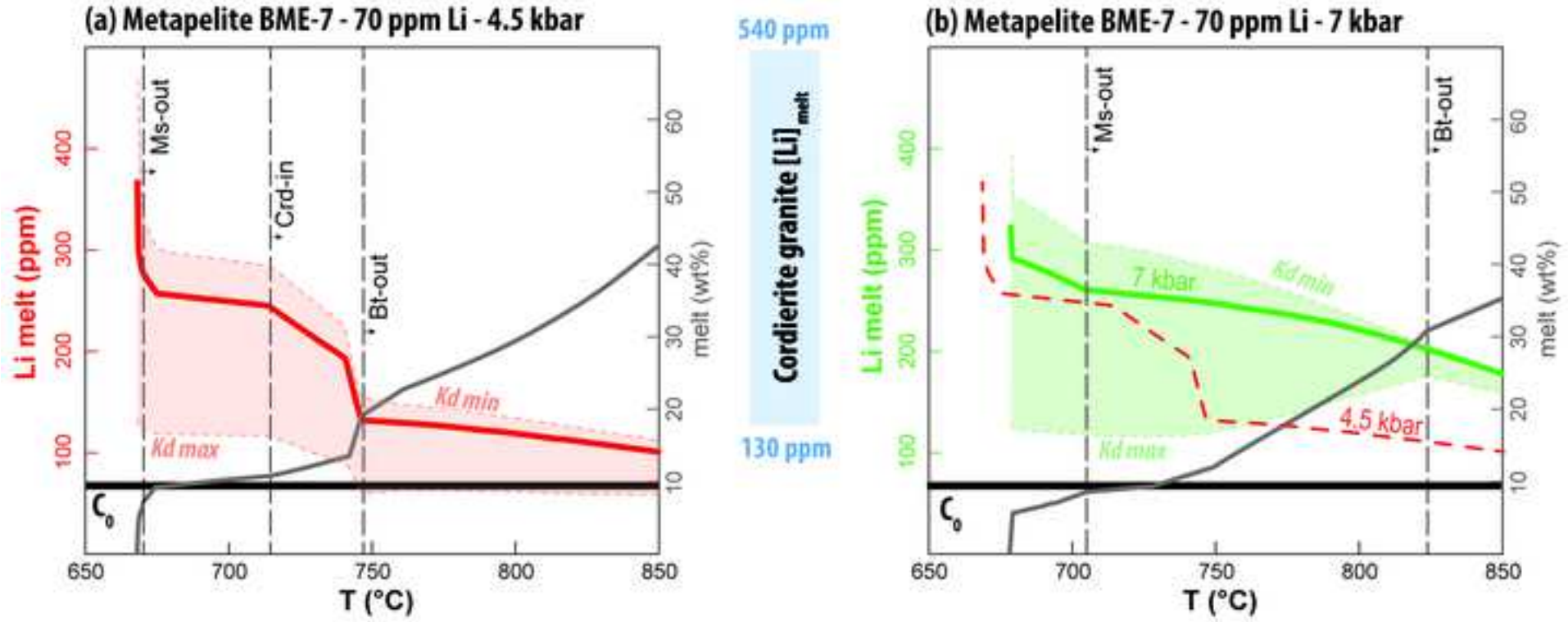

Figure 9

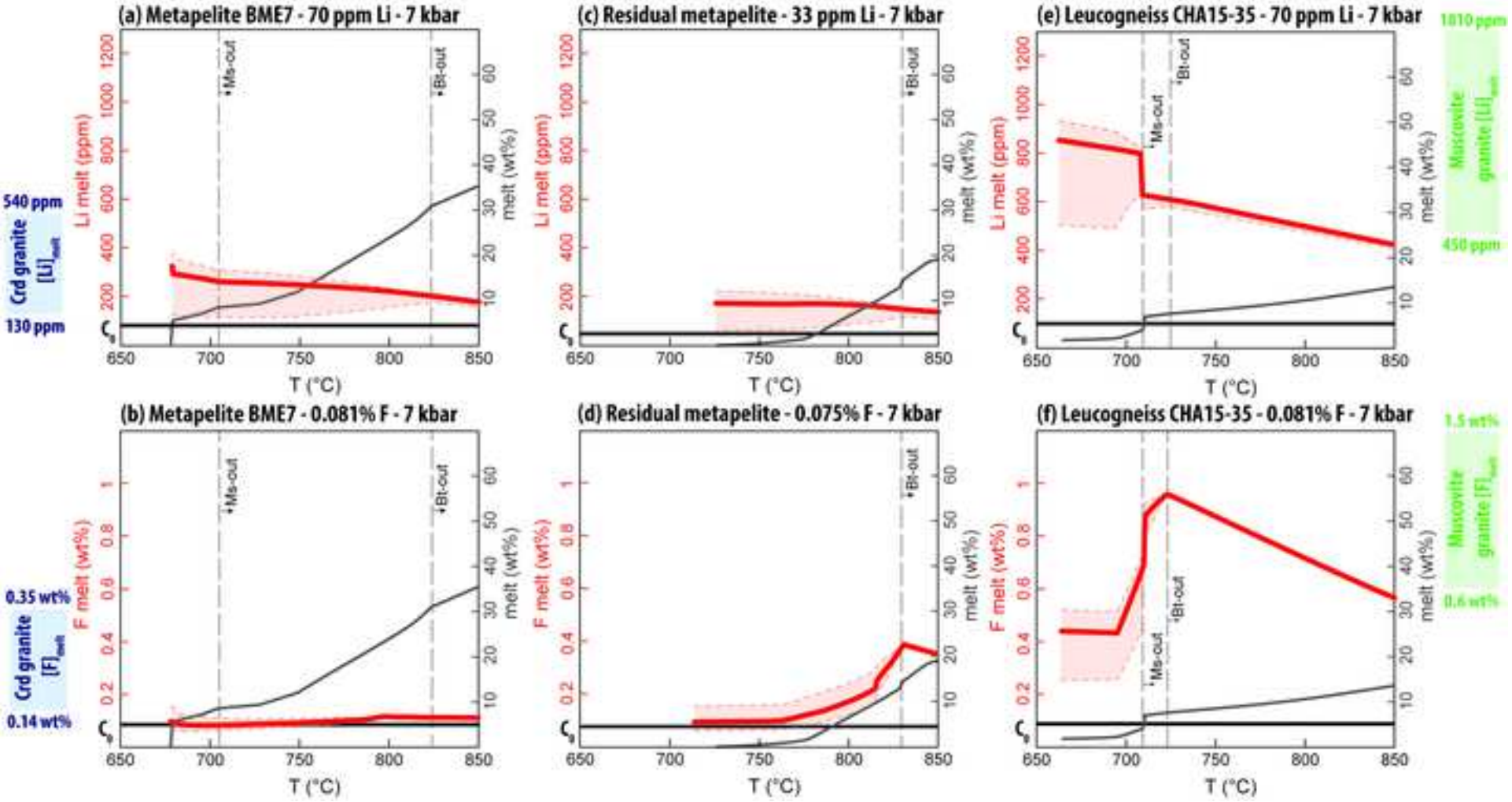

Figure 10

Click here to access/download;Figure;Fig.10-R1.tif

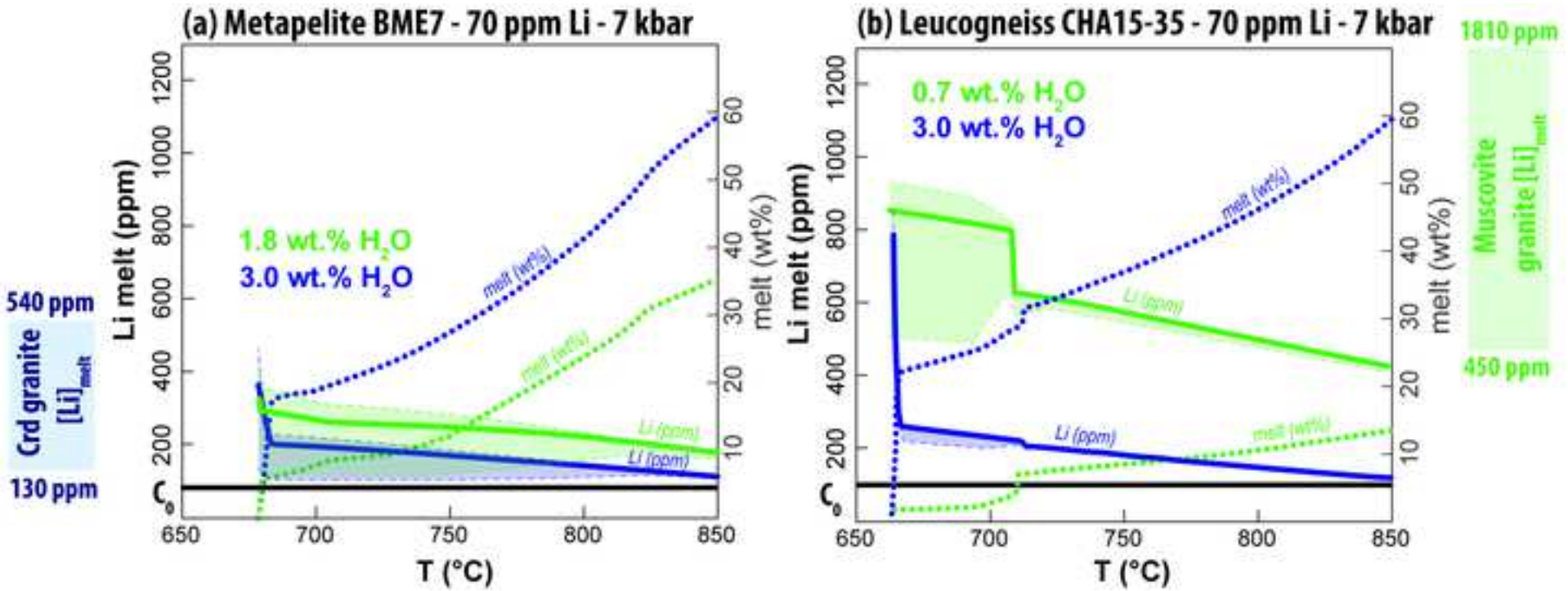

Figure 11

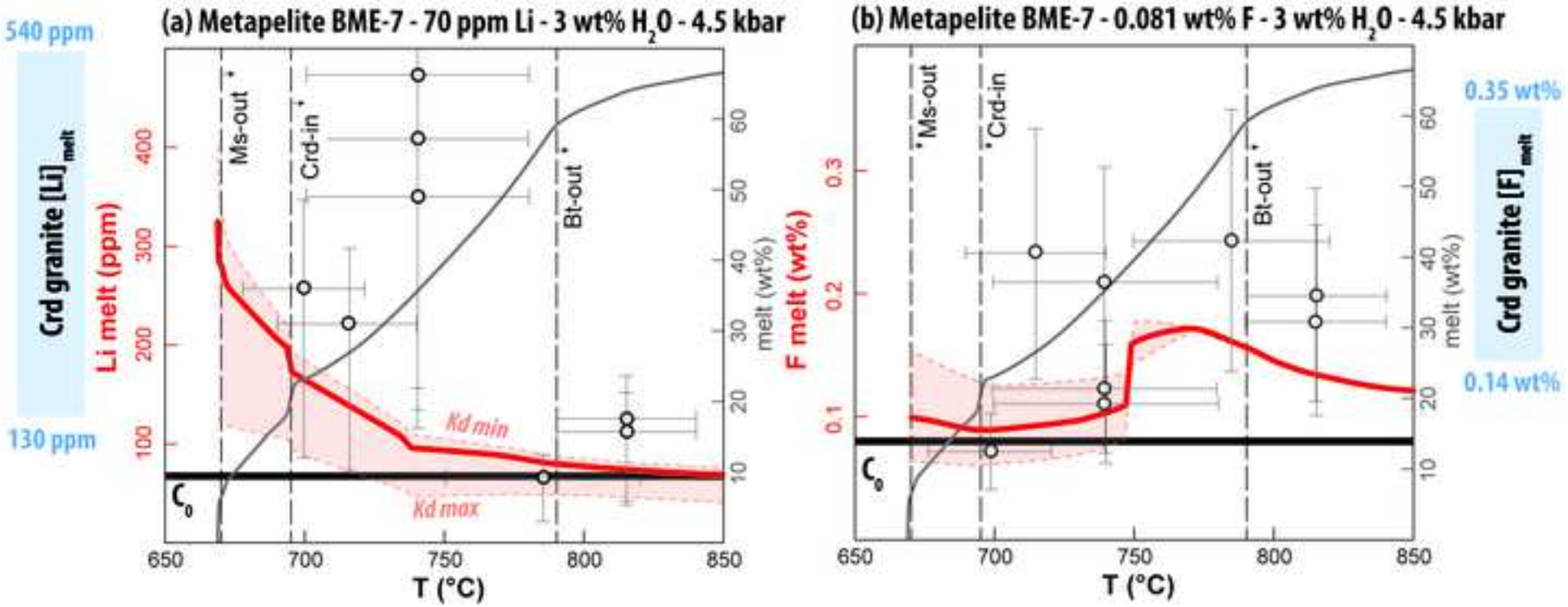

Figure 12

Click here to access/download;Figure;Fig.12-R1.tif

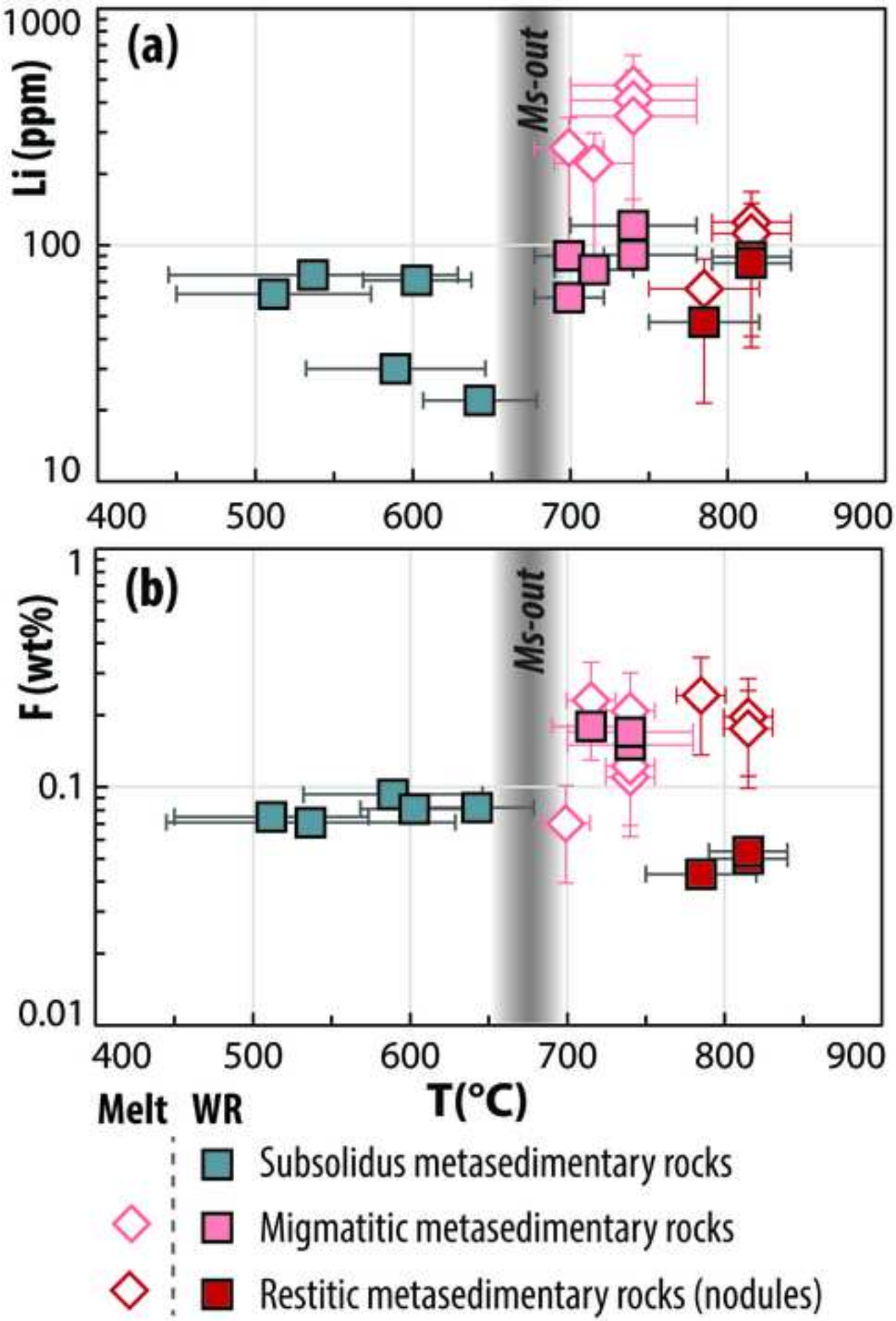

Figure 13

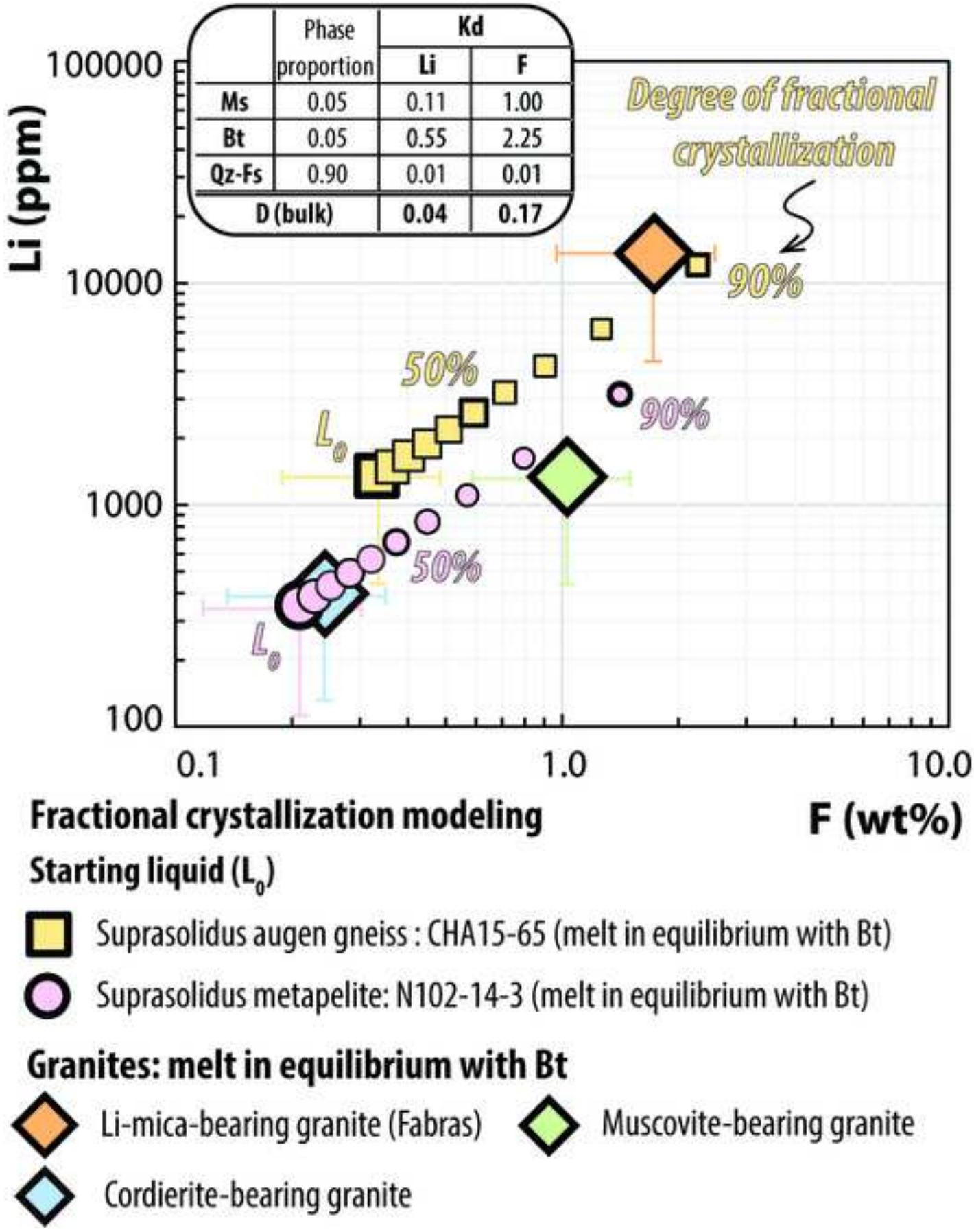

Table 1 Summary of P–T estimates obtained for the migmatites investigated in this study.

Sample	Ti-in-Bt (H05)	Ti-in-Bt ; *4.5±1.0 kbar* (W15)	Na-in-Crd (T18); *GASP (H01)*	Grt-Bt (H00); *GASP (H01)*	Grt-Crd (B93); *GASP (H01)*	Pseudosection analysis
PdB16-01a	699±22°C; n=16	647±53°C; n=16	-	-	-	-
MT11-6	704±29°C; n=37	669±58°C; n=37	-	-	-	700-770°C *< 4.6 kbar*
BAU21-3a	695±25°C; n=40	647±51°C; n=40	-	-	-	-
BAU21-3b	711±50°C; n=27	689±61°C; N=27	-	736°C *5.4 kbar*	-	700-780°C *> 5 kbar*
N102-14-3	717±7°C; n=15	711±22°C; n=15	-	-	-	690-780°C *< 4.5 kbar*
BO2	732±23°C; n=30	747±66°C; n=30	760±20°C; n=12 *> 4.4 kbar*	739°C *> 4.2 kbar*	753°C *> 4.3*	790-835°C *4-5 kbar*
BO3	736±20°C; n=18	744±42°C; n=18	761±19; n=17 *> 4.7 kbar*	723°C *> 4 kbar*	755°C *> 4.5 kbar*	790-835°C *4-5 kbar*
BO4	733±26°C; n=19	727±51°C; n=18	758±28°C; n=15 -	-	-	750-820°C *4-5 kbar*

H05 and W15 refer to the Ti-in-biotite thermometers of Henry et al. (2005) and Wu and Chen (2015), respectively. The italic values represent pressures calculated via the GASP barometer (Holdaway 2001) at temperatures obtained by Na-in-cordierite (Tropper et al. 2018), Grt-Bt (Holdaway 2000) and Grt-Crd (Bhattacharya 1993) thermometers. Uncertainties are two standard deviations. GASP barometry along with Grt-Bt and Grt-Crd thermometry relied on average mineral compositions calculated for each sample, as all minerals were chemically unzoned. When sillimanite is absent from the mineral assemblage, the calculated value represents a minimal pressure.

Table 2 Mineral-mineral partitioning data of Li and F for Velay samples.

Sample	Li									F		
	$Kd^{Bt/Ms}$	2σ (+)	2σ (-)	$Kd^{Crd/Bt}$	2σ (+)	2σ (-)	$Kd^{Bt/Grt}$	2σ (+)	2σ (-)	$Kd^{Bt/Ms}$	2σ (+)	2σ (-)
Subsolidus metasedimentary rock												
BME4	4.5	3.6	1.7	-	-	-	-	-	-	-	-	-
JOY14-2b	5.9	6.2	2.7	-	-	-	6.2	23.2	3.4	-	-	-
B15-1	2.4	1.5	0.8	-	-	-	-	-	-	-	-	-
BME6	16.9	9.3	5.0	-	-	-	-	-	-	-	-	-
BME7	11.7	3.7	2.6	-	-	-	-	-	-	-	-	-
Subsolidus Ordovician orthogneiss												
19CEZ04	2.7	0.9	0.6	-	-	-	-	-	-	-	-	-
Subsolidus Cadomian orthogneiss												
CHA15-35	5.0	2.8	1.5	-	-	-	-	-	-	1.8	1.3	0.6
Suprasolidus metasedimentary rock												
BAU21-3b	-	-	-	-	-	-	15.7	16.7	6.7	-	-	-
N102-14-3	-	-	-	1.8	0.9	0.6	-	-	-	-	-	-
B02	-	-	-	2.4	2.4	1.2	7.2	8.8	3.7	-	-	-
B04	-	-	-	2.8	2.5	1.6	-	-	-	-	-	-
B03	-	-	-	2.6	1.1	0.8	6.1	4.0	2.1	-	-	-
Suprasolidus Cadomian orthogneiss												
CHA15-65M	5.0	3.3	1.8	-	-	-	-	-	-	4.8	2.8	1.5
Cordierite-bearing granite												
PRL	-	-	-	1.3	0.9	0.6	-	-	-	-	-	-
Muscovite-bearing granite												
LV14-01	2.1	1.3	0.8	-	-	-	-	-	-	1.4	0.7	0.5
Li-mica-bearing granite												
ARD13-92a	3.6	4.5	1.5	-	-	-	-	-	-	1.5	1.0	0.5

Table 3 Partitioning data for Li and F used for partial melting models.

	Li			F		
	Min	Pref	*Max*	*Min*	Pref	*Max*
Kd $^{Bt/melt}$	0.41 [a]	0.55 [a]	1.67 [a]	1.56 [a]	2.25 [a]	4.00 [a]
Kd $^{Crd/Bt}$	-	2.00 [b]	-	-	-	-
Kd $^{Bt/Grt}$	-	6.00 [b]	-	-	-	-
Kd $^{Bt/Ms}$	-	5.00 [b]	-	-	-	-
Kd $^{Crd/melt}$	0.82 [c]	1.10 [c]	3.34 [c]	0.01 [d]	0.01 [d]	0.01 [d]
Kd $^{Grt/melt}$	0.07 [c]	0.09 [c]	0.28 [c]	0.01 [d]	0.01 [d]	0.01 [d]
Kd $^{Ms/melt}$	0.08 [c]	0.11 [c]	0.33 [c]	0.94 [a]	1.00 [a]	1.92 [a]

Pref: preferred; a: experimental Kd data compiled by Villaros and Pichavant (2019); b: values based on Velay rock samples (this study); c: values calculated using experimental Kd Bt/melt and Velay rock Kd mineral/mineral values; d: assumed values. The Kd of all other minerals was fixed to 0.01.